Time-resolved stimulated emission depletion and energy transfer dynamics in two-photon excited EGFP

Cite as: J. Chem. Phys. **148**, 134312 (2018); https://doi.org/10.1063/1.5011643 Submitted: 01 November 2017 • Accepted: 26 February 2018 • Published Online: 06 April 2018

T. A. Masters, D N. A. Robinson, R. J. Marsh, et al.









ARTICLES YOU MAY BE INTERESTED IN

Polarized two-photon photoselection in EGFP: Theory and experiment
The Journal of Chemical Physics 148, 134311 (2018); https://doi.org/10.1063/1.5011642

Invited Review Article: Pump-probe microscopy

Review of Scientific Instruments 87, 031101 (2016); https://doi.org/10.1063/1.4943211

Three dimensional live-cell STED microscopy at increased depth using a water immersion objective

Review of Scientific Instruments 89, 053701 (2018); https://doi.org/10.1063/1.5020249







Time-resolved stimulated emission depletion and energy transfer dynamics in two-photon excited EGFP

T. A. Masters, 1,2 N. A. Robinson, 1 R. J. Marsh, $^{1,a)}$ T. S. Blacker, 1,2 D. A. Armoogum, 1 B. Larijani, 3 and A. J. Bain $^{1,2,b)}$

(Received 1 November 2017; accepted 26 February 2018; published online 6 April 2018)

Time and polarization-resolved stimulated emission depletion (STED) measurements are used to investigate excited state evolution following the two-photon excitation of enhanced green fluorescent protein (EGFP). We employ a new approach for the accurate STED measurement of the hitherto unmeasured degree of hexadecapolar transition dipole moment alignment $\langle \alpha_{40} \rangle$ present at a given excitation-depletion (pump-dump) pulse separation. Time-resolved polarized fluorescence measurements as a function of pump-dump delay reveal the time evolution of $\langle \alpha_{40} \rangle$ to be considerably more rapid than predicted for isotropic rotational diffusion in EGFP. Additional depolarization by homo-Förster resonance energy transfer is investigated for both $\langle \alpha_{20} \rangle$ (quadrupolar) and $\langle \alpha_{40} \rangle$ transition dipole alignments. These results point to the utility of higher order dipole correlation measurements in the investigation of resonance energy transfer processes. © 2018 Author(s). All article content, except where otherwise noted, is licensed under a Creative Commons Attribution (CC BY) license (http://creativecommons.org/licenses/by/4.0/). https://doi.org/10.1063/1.5011643

I. INTRODUCTION

Stimulated emission depletion (STED) of electronically excited states has proven to be a valuable tool in high resolution molecular spectroscopy, in time-resolved spectroscopy,^{2–4} and in the study of ultrafast vibrational relaxation dynamics within ground and excited electronic states.^{5–7} In recent years, STED has found application in fluorescence microscopy, first as a pump-probe technique for time and polarization-resolved imaging⁸ and more extensively as a technique through which sub-wavelength image resolution can be achieved. 9-15 In parallel to these developments, we have shown that polarized time-resolved STED can be used to circumvent single-photon electric dipole selection rules 16 and allow the investigation of molecular orientation dynamics that are inaccessible to single photon spectroscopies. 17-21 In this work, we exploit this latter property of STED to observe hitherto "hidden" depolarization dynamics of the excited state hexadecapolar transition dipole alignment created by twophoton absorption (TPA) in enhanced green fluorescent protein (EGFP).

The degree of excited state order created by TPA is strongly dependent on both the photon polarization, the structure of the transition tensor and the molecular frame orientation of the transition dipole moment. ^{22–24} We have recently reported experimental measurements of polarized single- and

two-photon photoselection in EGFP which yield two possible transition tensor structures corresponding to the orientation of the principal axis along either the $S_0 \rightarrow S_1$ or $S_1 \rightarrow S_0$ transition moment directions.²⁵ These structures predict noticeably different values for the initial K=4 alignment which we determine in the present study.

Recent observations by us of state restriction in fluorescent protein Förster resonance energy transfer (FRET)²⁶ provide additional motivation for a detailed investigation into the interaction of fluorescent protein emission transition dipole moments with external optical fields. Most fluorescent proteins are characterised by bi-exponential fluorescence decays indicating the presence of two distinct excited state populations.^{26–30} A characterization of FRET between EGFP and mCherry arising from the homodimerization of 3-phosphoinositide-dependent protein kinase 1 (PDK1) has shown that only one of the four possible energy transfer pathways is active.²⁶ Two possible mechanisms for FRET restriction were proposed; first that the intrinsic energy transfer rates for the donor and acceptor sub-populations (proportional to their radiative decay rates given equal donor-acceptor distances and relative orientations) were widely dissimilar or second that the restriction arose from highly unfavourable κ^2 orientation factors³¹ caused by local environmental heterogeneities. Recent work in our laboratory has shown that both acceptor emitting states are accessed when EGFP is replaced with a more mobile and monoexponentially decaying donor.³² This indicates that in terms of the acceptor, intrinsic transition dipole strength is not an issue. FRET, spontaneous, and stimulated emission all share the same fundamental electric dipole selection rules. However, STED provides



¹Department of Physics and Astronomy, University College London, London WC1E 6BT, United Kingdom

²CoMPLEX, University College London, London WC1E 6BT, United Kingdom

³Cell Biophysics Laboratory, Ikerbasque, Basque Foundation for Science and Unidad de Biofisica (CSIC-UPV/EHU), Bilbao, Spain

a)Current address: Randall Division of Cell and Molecular Biophysics, New Hunt's House, King's College London, Guy's Campus, London SE1 1UL, United Kingdom.

b)Author to whom correspondence should be addressed: a.bain@ucl.ac.uk

a means of mimicking orientationally unrestricted (molecular frame) donor FRET photo-deselection (depletion) as the orientational dependence is governed solely by the photo-excitation process and the depletion polarization. Given the approximately equal weighting of the two decay components in EGFP, a large disparity in their transition dipole moments would be indicated by the persistence of a substantial "undumped" population, which, as will be seen, is not observed.

In this work, we employ a new streak camera-based approach for time and polarization-resolved STED measurements, allowing us to accurately determine the EGFP STED cross sections and ground state vibrational relaxation times for depletion wavelengths from 561 nm to 626 nm. An analysis of the orthogonally polarized components of the EGFP fluorescence allows us to extract the degree of K = 4 alignment that is present immediately prior to the application of the depletion pulse. By varying the pump-dump delay, we can determine the relaxation dynamics of this otherwise hidden degree of molecular alignment. The initial hexadecapolar alignment was found to be in line with the predictions of recent polarized twophoton absorption and fluorescence anisotropy measurements on EGFP.²⁵ However, we find the rate of hexadecapolar alignment relaxation to be significantly more rapid than would be expected for isotropic rotational diffusion. This is attributed to an increased rate of homo-FRET depolarization, pointing to the utility of such measurements as a more sensitive probe of energy transfer dynamics.

II. STED AS A PROBE OF HEXADECAPOLAR ALIGNMENT

A. Excited state orientational distribution function

Short pulsed polarized photoselection gives rise to an initial anisotropic distribution of molecular frame orientations in the laboratory frame of reference. In linearly polarized single and n-photon absorption, the excitation process has cylindrical symmetry about the polarization vector of the light $^{33-35}$ which defines the laboratory frame Z-axis. Emission from the excited population is characterised by a rearrangement of electronic charge in the molecular frame giving rise to a transition dipole moment. The probability of finding an emission transition dipole moment oriented between the polar angles θ and $\theta+\delta\theta$, and ϕ and $\phi+\delta\phi$ can be expressed in terms of a spherical harmonic expansion $^{36-38}$

$$P_{EX}\left(\theta,\phi,t=0\right) = \sum_{KQ} \left\langle C_{KQ}\left(0\right) \right\rangle Y_{KQ}\left(\theta,\phi\right). \tag{1}$$

The expansion coefficients $\langle C_{KQ}(0) \rangle$ define the moments of the distribution. As the excitation process has cylindrical symmetry about Z with an isotropic ground state population, this symmetry is transferred to the excited state distribution function and only even rank moments with Q=0 terms are allowed. As a result, the expansion can be fully described in terms of Legendre polynomials of rank K,

$$P_{EX}(x,t=0) = \frac{1}{2} \left[1 + \sum_{K>0} \frac{\left(1 + (-1)^K\right)}{2} \sqrt{2K + 1} \left\langle \alpha_{K0}(0) \right\rangle P_K(x) \right], \quad x = \cos\theta, \tag{2}$$

where $\langle \alpha_{K0}(0) \rangle$ are the normalized moments of the distribution

$$\langle \alpha_{K0}(0) \rangle = \langle C_{K0}(0) \rangle / \langle C_{00}(0) \rangle, \tag{3}$$

$$P_{EX}(x,t=0) = \frac{1}{2} \begin{bmatrix} 1 + \frac{\sqrt{5}}{2} \langle \alpha_{20}(0) \rangle \left(3x^2 - 1 \right) + \frac{3}{8} \langle \alpha_{40}(0) \rangle \left(35x^4 - 30x^2 + 3 \right) \\ + \frac{\sqrt{13}}{16} \langle \alpha_{40}(0) \rangle \left(231x^6 - 315x^4 + 105x^2 - 5 \right) + \cdots \end{bmatrix}. \tag{4}$$

The excited state (transition dipole) population distribution is given by

$$N_{EX}(x,t) = N_{EX}(t) P_{EX}(x,t),$$
 (5)

where $N_{EX}(t)$ is the total excited state population present at time t

For single-photon excitation from an isotropic ground state distribution, the expansion terminates at K=2. With two-photon excitation, the expansion contains both quadrupolar $(K=2, \langle \alpha_{20} \rangle)$ and hexadecapolar $(K=4, \langle \alpha_{40} \rangle)$ degrees of transition dipole alignment. The fluorescence anisotropy from the excited population is directly proportional to $\langle \alpha_{20} \rangle$, 36

$$R(t) = \langle \alpha_{20}(t) \rangle / \sqrt{5}. \tag{6}$$

Electric dipole selection rules do not allow the contribution of moments greater than K=2 in spontaneous emission, 36,37,39 and unlike $\langle \alpha_{20} \rangle$ the direct observation of $\langle \alpha_{40} \rangle$ is not possible. It has been known for some time that polarized single-photon absorption leads to coupling between the $\langle C_{00} \rangle$, $\langle C_{2Q} \rangle$, and $\langle C_{4Q} \rangle$ moments of the ground state orientational distribution and the $\langle C_{00} \rangle$ and $\langle C_{2Q} \rangle$ moments of the excited state distribution function. 36,37,39 Fluorescence anisotropy can therefore allow the measurement of steady state molecular order in both quantum rotors 40,41 and condensed phase molecular probes. 36,37,42 Linearly polarized two-photon dichroism directly relates ground state quadrupolar and hexadecapolar

alignment to the excited state population.^{34,43} However, the measurement of the dynamical evolution of higher order ground state alignment in the condensed phase is difficult; it is necessary to first create (with a definite time stamp) a distribution function with $\langle C_{K>2}, \rho \rangle$ moments that are displaced from their equilibrium values which can be combined with an appropriate measurement technique. Hole-burning techniques such as FRAP (fluorescence recovery after photobleaching)44,45 and ground state fluorescence depletion measurement⁴⁶ afford this possibility. The potential contribution of hexadecapolar alignment relaxation to these experiments has been recognized by some researchers⁴⁷ but with a view its removal from the recorded signals to provide more straightforward data analysis. An exception to this is a study by Dale and co-workers who used ground state orientational hole-burning through the population of long lived triplet states to probe $\langle \alpha_{20} \rangle$ and $\langle \alpha_{40} \rangle$ dynamics in muscle fibers. 46 Their technique, whilst well suited to its particular application, has an inherent limitation to microsecond time scales.

B. Higher order (hexadecapolar) molecular alignment

The paucity of direct measurement techniques by which higher order molecular alignment (both static and dynamic) can be probed has meant that, to date, studies of molecular order in gaseous and condensed phases have almost exclusively been confined to second order (K = 2) alignment observables. However, knowledge of higher degrees of molecular alignment provides new information that cannot otherwise be obtained. In molecular beam scattering of diatomic molecules from crystal surfaces, the measurement of the hexadecapolar alignment of the rotationally excited products provides additional and complimentary information to quadrupolar alignment, 48-50 and in two- and multiphoton molecular photodissociation the utility of measuring the higher order moments of the photofragment angular momentum M_I distributions has been recognized.^{51,52} In condensed phases, molecular ordering with moments of rank K > 2 is found in a wide range of environments, including liquid crystals, lipid bilayers, cell membranes, and at interfaces. 42,53-57

For isotropic solutions, in the case of small step rotational diffusion, the moments of $P_{EX}(x,t)$ evolve according to the diffusion equation. For a single axis symmetric rotational diffuser with diffusion coefficient D, this gives

$$\langle \alpha_{KQ}(t) \rangle = \langle \alpha_{KQ}(0) \rangle \exp[-DK(K+1)t].$$
 (7)

The evolution of an even ordered array of transition dipoles would therefore be

$$P_{EX}(x,t) = \frac{1}{2} \left[1 + \sum_{K>0} \left[\frac{\left(1 + (-1)^K\right)}{2} \sqrt{2K + 1} \times \langle \alpha_{K0}(0) \rangle \exp\left(\frac{-t}{\tau_{K0}}\right) P_K(x) \right] \right],$$
(8)

where

$$\tau_{20} = \frac{1}{6D}$$

$$\tau_{40} = \frac{1}{20D} = 0.3\tau_{20}$$

$$\vdots$$

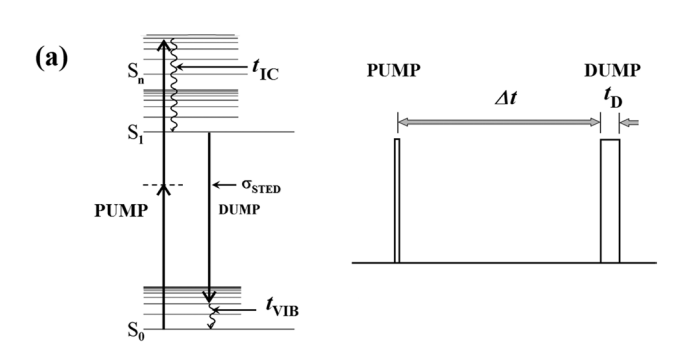
$$\tau_{K0} = \frac{6}{K(K+1)}\tau_{20}$$
(9)

Knowledge of one correlation function should therefore yield the others. This relationship had not been tested experimentally until the development and subsequent application of six wave mixing techniques by Charra et al. 60-62 and Meech and coworkers.⁶³ Here, non-centrosymmetric molecular order characterized by K = 1 (dipolar alignment or orientation) and K = 3 (octupolar alignment) is created and probed in a 4th order nonlinear optical mixing process with pump and probe fields at ω and 2ω . If molecular motion is no longer diffusive (e.g., co-operative), Eq. (7) no longer applies and the time evolution of moments in addition to $\langle \alpha_{20} \rangle$ will provide new information and test dynamical theories. 64,65 Dipolar (K = 1) correlation functions in neat liquids can be inferred from infrared lineshape measurements^{66,67} and in recent years have been directly probed by femtosecond domain techniques such as TFISH (terahertz field induced second harmonic generation).⁶⁸ The presence of hexadecapolar order in liquid crystal and membrane environments has been shown to influence the orientational dynamics of fluorescent probes measured through $\langle \alpha_{20}(t) \rangle$. 22,55,69–72

Resonance energy transfer is also a well-known fluorescence depolarization mechanism. 73–76 In the case of transfer between identical molecules (homo-FRET), migration of the initial excitation to surrounding molecules leads to a partial (time-dependent) randomization of the emission dipole moment alignment in the laboratory frame. Homo-FRET fluorescence depolarization has been investigated in Langmuir-Blodgett films^{77,78} and between rigidly held⁷⁹ and rotationally diffusing^{80,81} molecules. To date, we are unaware of any measurement or theoretical modeling of FRET depolarization (homo- or hetero-transfer) that extends beyond transition dipole moment correlation functions of rank K = 2. Given the greater sensitivity of $\langle \alpha_{40} \rangle$ to small step angular averaging as compared to $\langle \alpha_{20} \rangle$ [see Eq. (9)], it is reasonable to expect that the degree of hexadecapolar depolarization due to energy migration will be more pronounced, affording the possibility of detecting and potentially quantifying energy transfer dynamics at lower concentrations (greater intermolecular distances) than permitted by conventional fluorescence anisotropy measurements. In addition, we have recently demonstrated the greater dependence of the initial hexadecapolar alignment created by TPA to the transition tensor structure and the emission transition dipole moment direction in the molecular frame.²⁵ Determining the initial hexadecapolar alignment and its ensuing evolution therefore has the potential to provide important spectroscopic information and yield new insight into excited state dynamics.

C. Time-resolved pulsed STED observables

A schematic Jablonski diagram illustrating the principles of two-photon excited STED in EGFP is shown in Fig. 1(a). Two-photon excitation via an 800 nm (200 fs) laser pulse (pump) is followed by rapid radiationless relaxation (t_{IC}) to lower vibrational levels of the S₁ singlet state in accordance with Kasha's rule. 82 Spontaneous emission to Franck-Condon allowed vibrational levels in So gives rise to a broad emission spectrum peaking at around 508 nm with fluorescence detectable out to approximately 640 nm. 83 Application of a time delayed (Δt) dump pulse leads to the preferential photodeselection of molecules whose transition dipole moments are closely aligned to the dump polarization. As a result, there is an abrupt change in the fluorescence anisotropy in addition to the polarized and total fluorescence intensities. The efficiency of STED is, in addition to the STED cross section and orientational factors, dependent on the depopulation rate $(1/t_{VIB})$ of the terminating vibrational levels in S₀ compared to the duration of the dump pulse (t_D) . If t_D is shorter or comparable to t_{VIB} , re-pumping of S_1 becomes more marked with increasing dump energy and the degrees of population depletion and fluorescence depolarization are seen to saturate. 16,19 Typical results for EGFP illustrating this behavior are shown in Fig. 2, together with the polarized fluorescence and anisotropy measurements used to determine the alignment dynamics.



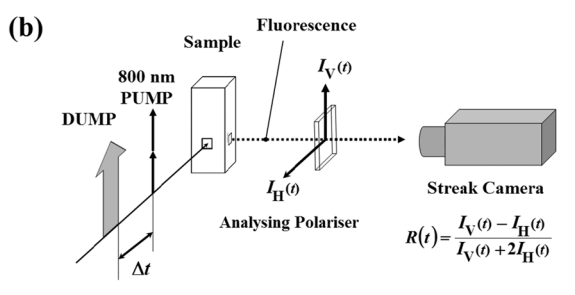


FIG. 1. (a) Spontaneous and STED induced photophysical pathways in a population of fluorescent probes following near infrared TPA (pump pulse). Following linearly polarized TPA, there is rapid (sub-ps) relaxation to low lying vibrational levels of $S_1.$ At an experimentally variable time $\varDelta t$ following TPA, a linearly polarized dump pulse is applied which removes population from $S_1.$ (b) Measurement of fluorescence observables: the time-resolved intensities for fluorescence polarized parallel (V) and perpendicular (H) to the excitation pulse are recorded by imaging the depletion region onto the entrance slit of a streak camera allowing the evolution of the $S_1 \rightarrow S_0$ fluorescence prior to, during, and after the application of the dump pulse.

D. Orientational photo-deselection in STED

In spite of the widespread application of STED as an imaging technique, ⁸⁴ there has been little experimental or theoretical work aimed at characterizing the fundamental physics of the depletion process. It is therefore instructive to investigate the two principal mechanisms operating in pulsed STED from large (slowly reorienting) molecules: orientational photo-deselection and excited state re-pumping. First, to focus upon orientational photo-deselection, we examine the limit of very fast ground state relaxation, where re-pumping of the excited state during the application of a picosecond range dump pulse can be neglected. In EGFP, molecular rotation and spontaneous emission occur on a significantly slower time scale [τ_F (average) = 2.75 ns, τ_{20} = 19.5 ns] and can be neglected during the depletion process. The evolution of the excited state population distribution is then given by

$$\frac{\partial N_{EX}(x,t)}{\partial t} = -\left(\frac{\sigma_{STED}I(t)x^2}{h\nu_D}\right)N_{EX}(x,t), \quad (10)$$

where σ_{STED} is the stimulated emission cross section, I(t) is the depletion pulse intensity, $h\nu_D$ is the dump photon energy, and $x = \cos\theta$, with θ being the angle between the emission transition dipole moment and the polarization vector of the dump pulse.

If we approximate the dump pulse to have a constant intensity for duration t_D and is applied at a time Δt following excitation, integration of Eq. (10) yields

$$N_{EX}(x, \Delta t + t_D) = N_{EX}(x, \Delta t) \exp\left(-Sx^2\right), \quad S = \frac{\sigma_{STED}E_D}{Ah\nu_D},$$
(11)

where $E_D/Ah\nu_D$ is the flux of dump photons (photons cm⁻²) for a dump pulse of energy E_D and area A. The transition dipole moment probability distributions are thus

$$P_{EX}(x, \Delta t + t_D) = \frac{N_{EX}(\Delta t)}{N_{EX}(\Delta t + t_D)} P_{EX}(x, \Delta t) \exp\left(-Sx^2\right).$$
(12)

With two-photon excitation, the excited state distribution function terminates at K=4. The transition dipole probability distribution in the absence of the dump pulse can then be written as

$$P_{EX}(x,t) = \frac{1}{2} \left[1 + \frac{5}{2}R(t)(3x^2 - 1) + \langle \alpha_{40}(t) \rangle \frac{3}{8} (35x^4 - 30x^2 + 3) \right].$$
 (13)

The fluorescence observables $I_V(t)$ and $I_H(t)$ (see Fig. 1) immediately prior to the application of the dump pulse are given by

$$I_{V}(\Delta t) = CN_{EX}(\Delta t) \int_{-1}^{1} P_{EX}(x, \Delta t) x^{2} dx, \qquad (14)$$

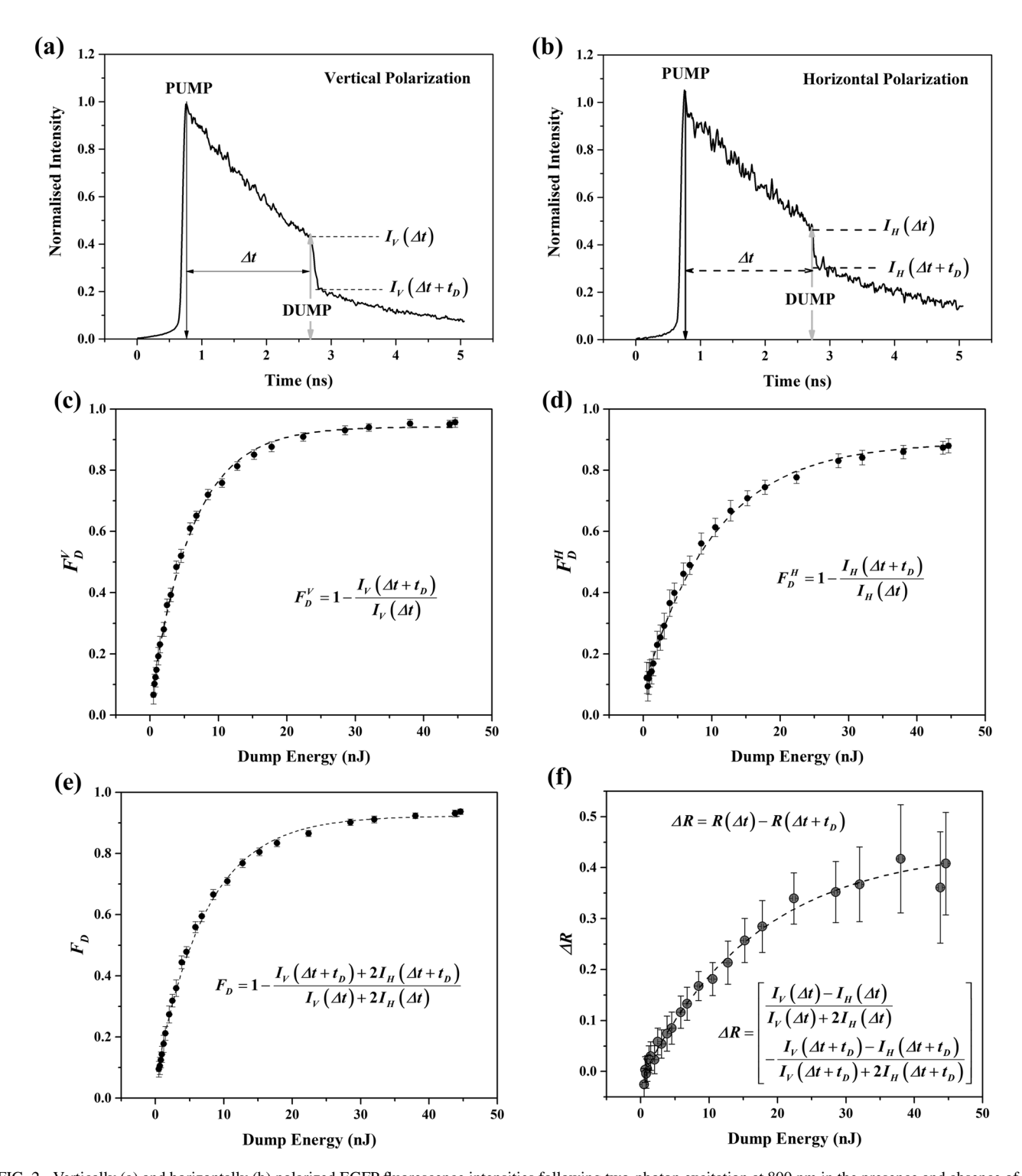


FIG. 2. Vertically (a) and horizontally (b) polarized EGFP fluorescence intensities following two-photon excitation at 800 nm in the presence and absence of a time delayed (2 ns) dump pulse. The application of the dump pulse leads to a sharp decrease in the polarized emission intensities from which the total degree of population removal F_D and the net change (decrease) in emission anisotropy ΔR together with the intrinsic degrees of polarized depletion F_D^V and F_D^H are determined. Variation in these quantities with dump pulse energy is shown in (c)–(f). The dashed lines through the data points are nonlinear least square fits using single exponential growth functions and are shown solely as a guide to the eye.

$$I_{H}(\Delta t) = CN_{EX}(\Delta t) \int_{-1}^{1} P_{EX}(x, \Delta t) \frac{1}{2} (1 - x^{2}) dx, \quad (15)$$

$$I_{V}(\Delta t) = CN_{EX}(\Delta t) \frac{2}{3} [1 + 2R(\Delta t)], \quad (16)$$

$$I_{H}(\Delta t) = CN_{EX}(\Delta t) \frac{2}{3} [1 - R(\Delta t)]. \quad (17)$$

where C is a constant of proportionality. Equations (14) and (15) have simple analytic forms,

Immediately after the application of the dump pulse I_V , I_H and the fluorescence anisotropy become

$$I_{V}(\Delta t + t_{D}) = CN_{EX}(t_{D}) \int_{-1}^{1} P_{EX}(x, \Delta t) \exp\left(-Sx^{2}\right) x^{2} dx,$$

$$(18)$$

$$CN_{EX}(\Delta t) \int_{-1}^{1} P_{EX}(x, \Delta t) \exp\left(-Sx^{2}\right) x^{2} dx,$$

$$I_{H}(\Delta t + t_{D}) = \frac{CN_{EX}(\Delta t)}{2} \int_{-1}^{1} P_{EX}(x, \Delta t)$$

$$\times \exp(-Sx^{2}) (1 - x^{2}) dx, \tag{19}$$

$$R(\Delta t + t_D) = \frac{\int_{-1}^{1} P_{ex}(\Delta t) \exp(-Sx^2) \frac{1}{2} (3x^2 - 1) dx}{\int_{-1}^{1} P_{ex}(\Delta t) (-Sx^2) dx}.$$
 (20)

Rewriting the transition dipole probability distribution in terms of powers of x, we have

$$P_{EX}(x,t) = \frac{1}{2} \left[A(t) + B(t) x^{2} + C(t) x^{4} \right],$$

$$A(t) = \left(1 - \frac{5}{2} R(t) + \frac{9}{8} \langle \alpha_{40}(t) \rangle \right),$$

$$B(t) = \left(\frac{15}{2} R(t) - \frac{90}{8} \langle \alpha_{40}(t) \rangle \right),$$

$$C(t) = \left(\frac{105}{8} \langle \alpha_{40}(t) \rangle \right).$$
(21)

Using this format, Eqs. (18)–(20) become

$$I_{V}(\Delta t + t_{D}) = \frac{CN_{EX}(\Delta t)}{2} \left[A_{2}A(\Delta t) + A_{4}B(\Delta t) + A_{6}C(\Delta t) \right], \tag{22}$$

$$I_{H}(\Delta t + t_{D}) = \frac{CN_{EX}(\Delta t)}{4} \begin{bmatrix} A_{0}A(\Delta t) + A_{2} \left[B(\Delta t) - A(\Delta t) \right] \\ +A_{4} \left[C(\Delta t) - B(\Delta t) \right] - A_{6}C(\Delta t) \end{bmatrix}, \tag{23}$$

$$R(\Delta t + t_D) = \frac{-A(\Delta t)A_0 + (3A(\Delta t) - B(\Delta t))A_2 + (3C(\Delta t) - B(\Delta t))A_4 - 3C(\Delta t)A_6}{A(\Delta t)A_0 + B(\Delta t)A_2 + C(\Delta t)A_3}.$$
 (24)

In the above, A_n are standard Gaussian integrals of the form (see the Appendix)

$$A_n = \int_{-1}^{1} x^n \exp\left(-Sx^2\right) dx. \tag{25}$$

With this approach, the fluorescence depletion parameters are

$$F_D = 1 - \frac{I_V(\Delta t + t_D) + 2I_H(\Delta t + t_D)}{I_V(\Delta t) + 2I_H(\Delta t)} = 1 - \left[\frac{A(\Delta t)A_0 + B(\Delta t)A_2 + C(\Delta t)A_4}{2} \right],$$
(26)

$$F_D^V = 1 - \frac{I_V(\Delta t + t_D)}{I_V(\Delta t)} = 1 - \frac{A(\Delta t)A_2 + B(\Delta t)A_4 + C(\Delta t)A_6}{\frac{2}{3}A(\Delta t) + \frac{2}{5}B(\Delta t) + \frac{2}{7}C(\Delta t)},$$
(27)

$$F_{D}^{V} = 1 - \frac{I_{V}(\Delta t + t_{D})}{I_{V}(\Delta t)} = 1 - \frac{A(\Delta t)A_{2} + B(\Delta t)A_{4} + C(\Delta t)A_{6}}{\frac{2}{3}A(\Delta t) + \frac{2}{5}B(\Delta t) + \frac{2}{7}C(\Delta t)},$$

$$F_{D}^{H} = 1 - \frac{I_{H}(\Delta t + t_{D})}{I_{H}(\Delta t)} = 1 - \frac{A_{0}A(\Delta t) + A_{2}[B(\Delta t) - A(\Delta t)] + A_{4}[C(\Delta t) - B(\Delta t)] - A_{6}C(\Delta t)}{2A(\Delta t) + \frac{2}{3}[B(\Delta t) - A(\Delta t)] + \frac{2}{5}[C(\Delta t) - B(\Delta t)] - \frac{2}{7}C(\Delta t)}.$$
(28)

Similarly the net change in fluorescence anisotropy is

$$\Delta R = R \left(\Delta t + t \right) - \left[\frac{-A \left(\Delta t \right) A_0 + \left[3A \left(\Delta t \right) - B \left(\Delta t \right) \right] A_2 + \left[3B \left(\Delta t \right) - C \left(\Delta t \right) \right] A_4 + 3C \left(\Delta t \right) A_6}{2 \left[A \left(\Delta t \right) A_0 + B \left(\Delta t \right) A_2 + C \left(\Delta t \right) A_4 \right]} \right]. \tag{29}$$

Plots of F_D , F_D^V , F_D^H , and ΔR as a function of S are shown in Fig. 3. In Fig. 3(a), F_D shows a rapid increase to 91% over the range of S = 0-4. With higher dump energies, there is a significant downturn in the degree of removal of the remaining population whose transition dipole moment orientations are less favourably aligned with the dump pulse polarization. In Fig. 3(b), the degree of depletion as measured by the vertical and horizontally polarized emission intensities $(F_D^V \text{ and } F_D^H)$ is compared to F_D . The intensity of vertically polarized fluorescence has a larger contribution from molecules whose transition dipole moments have a preferential alignment to the dump polarization as compared to the total fluorescence intensity and as a result shows a greater degree of initial depletion with S. Conversely, for horizontally polarized fluorescence, the dominant contribution to the emission

intensity is largely derived from transition dipole moments preferentially aligned in the plane orthogonal to the dump polarization, therefore showing the lowest degree of depletion. F_D^V, F_D , and F_D^H begin to converge once significant population depletion and depolarization have occurred. At the point where the post dump fluorescence anisotropy has been reduced from 4/7 to zero ($S \approx 7.27$), the values of F_D^V , F_D and F_D^H are 0.9892, 0.9769, and 0.9462, respectively. At S = 17.5, $\Delta R = 6/7$ and the surviving population has a fluorescence anisotropy of -2/7. This is equivalent to all of the initially photo-excited molecules experiencing a transition dipole moment reorientation of 90°. Here, the necessary population removal is extremely high $(F_D = 0.99741)$. The limiting value for ΔR of 15/14 [Fig. 3(c)] corresponds to depletion resulting in a totally STED resistant population of transition dipole moments oriented at an angle of

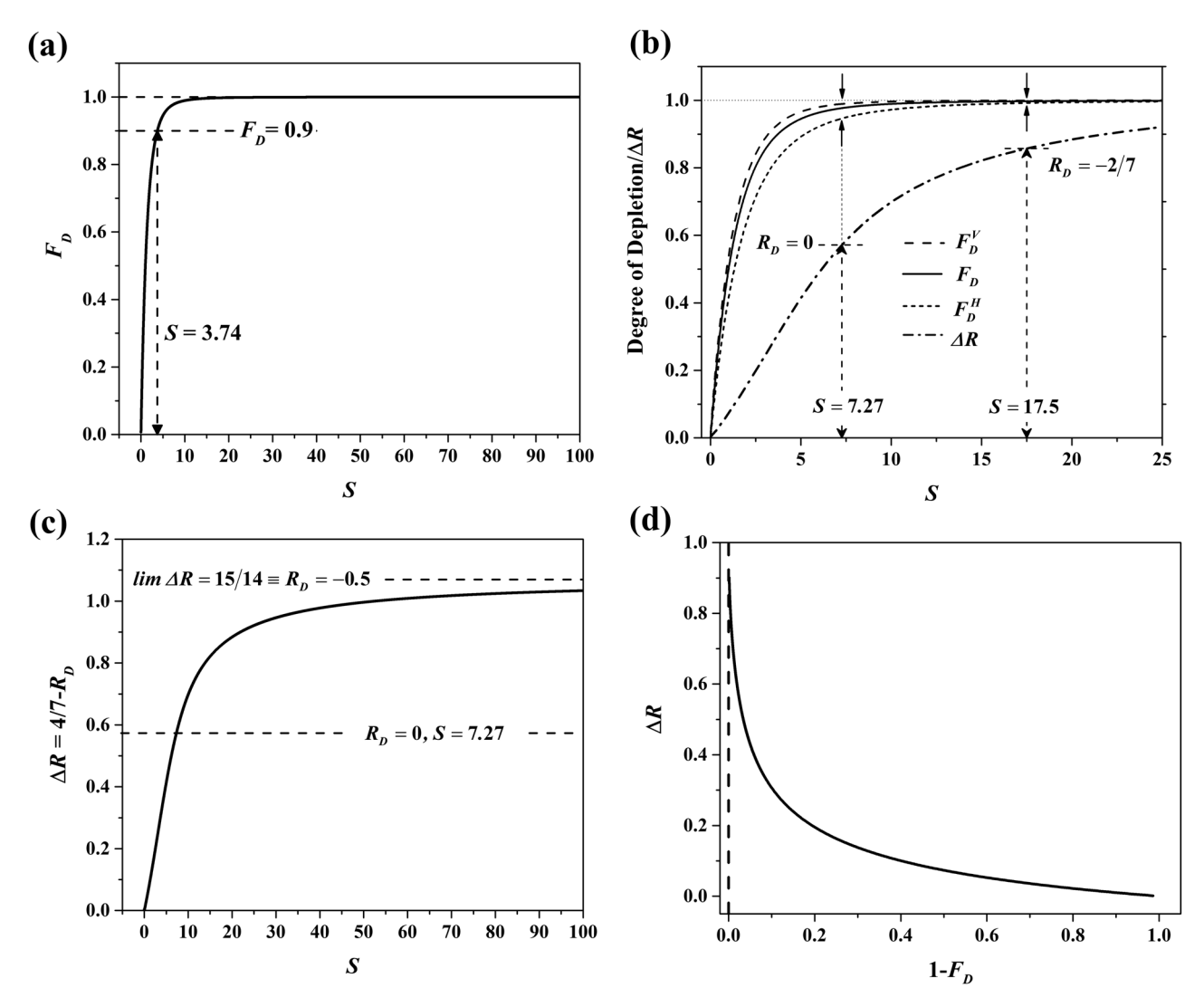


FIG. 3. [(a)-(c)] Simulation of F_D , F_D^V , F_D^H , and ΔR with dump energy ($S = \sigma_{STED}E_{DUMP}/Ahv_D$), for a population of two-photon excited molecules with an initial $\cos^4\theta$ orientational distribution in the limit of fast ground state relaxation. (b) compares F_D , F_D^V , F_D^H , and ΔR for dump energies up to S = 25; the greatest degree of depletion is observed for F_D^V . (c) shows the change in the fluorescence anisotropy for values of S up to 100 where the theoretical limit of 15/14 is approached to within 3.5%. (d) Correlation between the degree of population remaining in the upper level $(1 - F_D)$ and the change in anisotropy ΔR induced by the dump pulse.

exactly 90° to the dump polarization, approached in the region of S=100. However, this limit is unphysical as the excited state population is not totally static during the depletion process and a residual population (however small) exhibiting a δ -function angular distribution is never achieved. Figure 3(d) shows the correlation between the degree of population surviving STED $(1-F_D)$ and the induced anisotropy change (ΔR) . In the limit of moderate depletion $(1-F_D>0.6)$, the relationship is approximately linear with a gradient of -0.13 ($R^2=0.99$).

E. STED dynamics with excited state repumping

The representative STED data displayed in Fig. 2 exhibit decreasing degrees of depletion and induced anisotropy change with increasing dump energy. It is notable that [Fig. 2(c)] F_D reaches an approximate plateau of 93% and

[Fig. 2(f)] it is not possible to drive the dumped anisotropy below zero (at $\Delta t = 2$ ns $R_U \approx 0.5$). This indicates that the saturation of these quantities is not purely based on the persistence of a STED resistant population of unfavorably oriented transition dipole moments. The increase in the degree of depletion efficiency with dump pulse width observed in previous STED studies of fluorescent probes 16 is further indication that excited state re-pumping during the application of the dump pulse cannot be ignored in any accurate analysis. A solution of the coupled rate equations is therefore required. ¹⁶ In our experiments, the picosecond time scale of STED is significantly shorter than both the molecular reorientation and fluorescence lifetimes of EGFP (as discussed above), and these contributions to the depletion dynamics can be neglected. With the (sole) approximation of a constant dump intensity over a time duration t_D , the evolution of the excited $N_{EX}(x,t)$ and upper vibrational $N_{GS}(x,t)$ ground state populations is given by

$$\frac{\partial N_{EX}(x,t)}{\partial t} = \frac{Sx^2}{t_D} \left(N_{GS}(x,t) - N_{EX}(x,t) \right), \qquad (30)$$

$$\frac{\partial N_{GS}(x,t)}{\partial t} = \frac{Sx^2}{t_D} \left(N_{EX}(x,t) - N_{GS}(x,t) \right) - \frac{1}{t_{VIB}} N_{GS}(x,t).$$
(31)

The initial population distribution in the upper ground state vibrational levels is negligible $[N_{GS}(x,0) = 0]$ and the excited state population evaluated at $t = \Delta t + t_D$ is given by

$$N_{EX}(x, \Delta t + t_D) = N_{EX}(\Delta t) P_{EX}(x, \Delta t) \times G_{DUMP},$$

$$G_{DUMP} = \left[\frac{\exp\left(-\left(t_D/t_{VIB} + 2Sx^2 + d\right)/2\right)}{2d}\right]$$

$$\times \left[\frac{t_D}{t_{VIB}}(\exp(d) - 1)\right].$$

$$+d(\exp(d) + 1)$$
(32)

The parameter d is

$$d = \sqrt{(t_D/t_{VIB})^2 + 4S^2x^4}. (33)$$

In the limit where t_D/t_{VIB} is large, Eq. (32) tends to Eq. (11). The STED observables are thus

$$F_{D} = 1 - \frac{\int_{-1}^{1} G_{DUMP} N_{EX}(x, \Delta t) dx}{\int_{-1}^{1} N_{EX}(x, \Delta t) dx},$$
 (34)

$$F_D^V = 1 - \frac{\int_{-1}^{1} G_{DUMP} N_{EX}(x, \Delta t) x^2 dx}{\int_{-1}^{1} N_{EX}(x, \Delta t) x^2 dx},$$
 (35)

$$F_D^H = 1 - \frac{\int_{-1}^{1} G_{DUMP} N_{EX}(x, \Delta t) \left(1 - x^2\right) dx}{\int_{-1}^{1} N_{EX}(x, \Delta t) \left(1 - x^2\right) dx},$$
 (36)

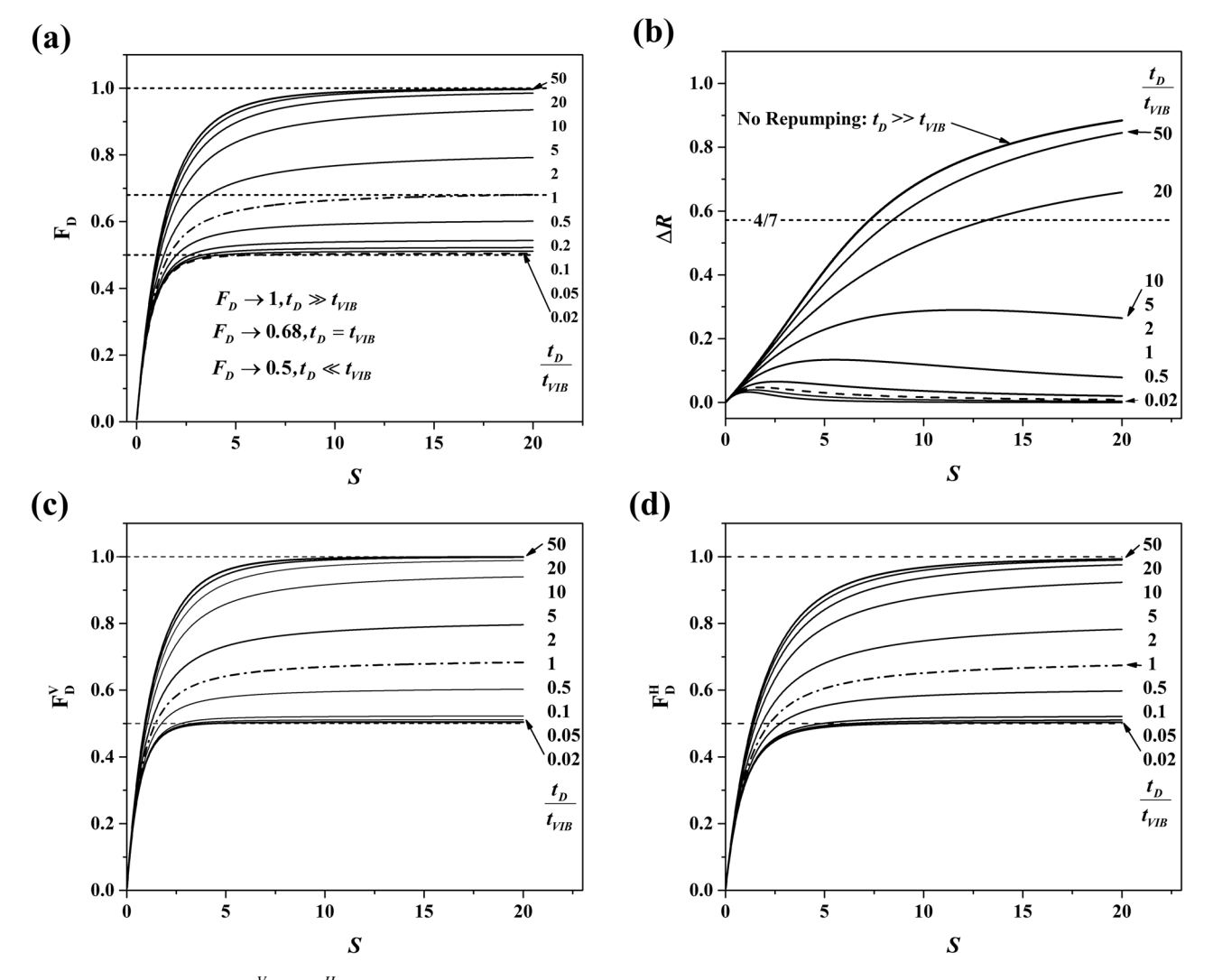


FIG. 4. Simulation of F_D , ΔR , F_D^V , and F_D^H against dump energy ($S = \sigma_{STED}E_{DUMP}/Ahv_D$), for a population of two-photon excited molecules with an initial $\cos^4 \theta$ orientational distribution $[\langle \alpha_{20}(\Delta t=0)\rangle = (4/7)\sqrt{5}, \langle \alpha_{40}(\Delta t=0)\rangle = 8/21]$ as a function of t_D/t_{VIB} , the dump pulse width to ground state relaxation time ratio. With increasing t_D/t_{VIB} , the degree of depletion and change in dump-induced fluorescence anisotropy are maximized. F_D , F_D^V , and F_D^H are seen to plateau (saturate) in the region of S > 6 with close to 100% depletion achieved in the region where $t_D/t_{VIB} \approx 50$.

$$\Delta R = R(\Delta t) - \frac{\frac{1}{2} \int_{-1}^{1} G_{DUMP} N_{EX}(x, \Delta t) \left(3x^{2} - 1\right) dx}{\int_{-1}^{1} G_{DUMP} N_{EX}(x, \Delta t) dx}.$$
 (37)

The integrals in Eqs. (34)–(37) were calculated using Mathematica (Wolfram Research), first to generate qualitative fluorescence intensity depletion and fluorescence anisotropy curves and second, with variable input parameters, for quantitative analysis of the experimental data. Figure 4 shows simulations of Eqs. (34)–(37) as a function of S for values of t_D/t_{VIB} ranging from 50 to 0.02 for a two-photon excited population with initial anisotropy and hexadecapolar alignment of 4/7 and 8/21, respectively. Population depletion and depolarization are both maximized with increasing t_D/t_{VIB} ; F_D , F_D^V , and F_D^H are seen to plateau (saturate) in the region where S>6 with close to 100% depletion achieved when $t_D/t_{VIB}\approx 50$. The maximum degree of population depletion attainable decreases as t_D/t_{VIB} is reduced. When t_D and t_{VIB} are equal, this is approximately 0.68. When $t_{VIB}\gg t_D$, the population removed as the dump

pulse is applied becomes bottlenecked in the upper ground state vibrational levels and the maximum degree of population depletion that is attainable tends to 0.5. This is analogous to the limit observed in the continuous wave optical pumping of a two-level system in the absence of spontaneous emission.85 The change in fluorescence anisotropy shows a high degree of sensitivity to the degree of excited state re-pumping. When $t_D/t_{VIB} = 50$, the change in fluorescence anisotropy closely follows that observed in the limit of no excited state repumping. As t_D/t_{VIB} decreases, the anisotropy no longer rises with increasing S but reaches a plateau and then decreases. When $t_D/t_{VIB} = 10$, the maximum anisotropy change that can be induced is 0.29 (S = 11.62). When t_D/t_{VIB} = 1, this reduces to approximately 0.047 (S = 1.68). At lower values of t_D/t_{VIB} , this form of the induced anisotropy is retained with a lower peak in ΔR occurring at a lower value of $S(t_D/t_{VIB} = 0.02$, $\Delta R = 3.29 \times 10^{-2}$, and S = 1.14) with ΔR tending toward zero thereafter. With a population bottleneck in the lower level and in the absence of orientational relaxation, re-pumping of the excited state simply replaces the molecular transition dipole

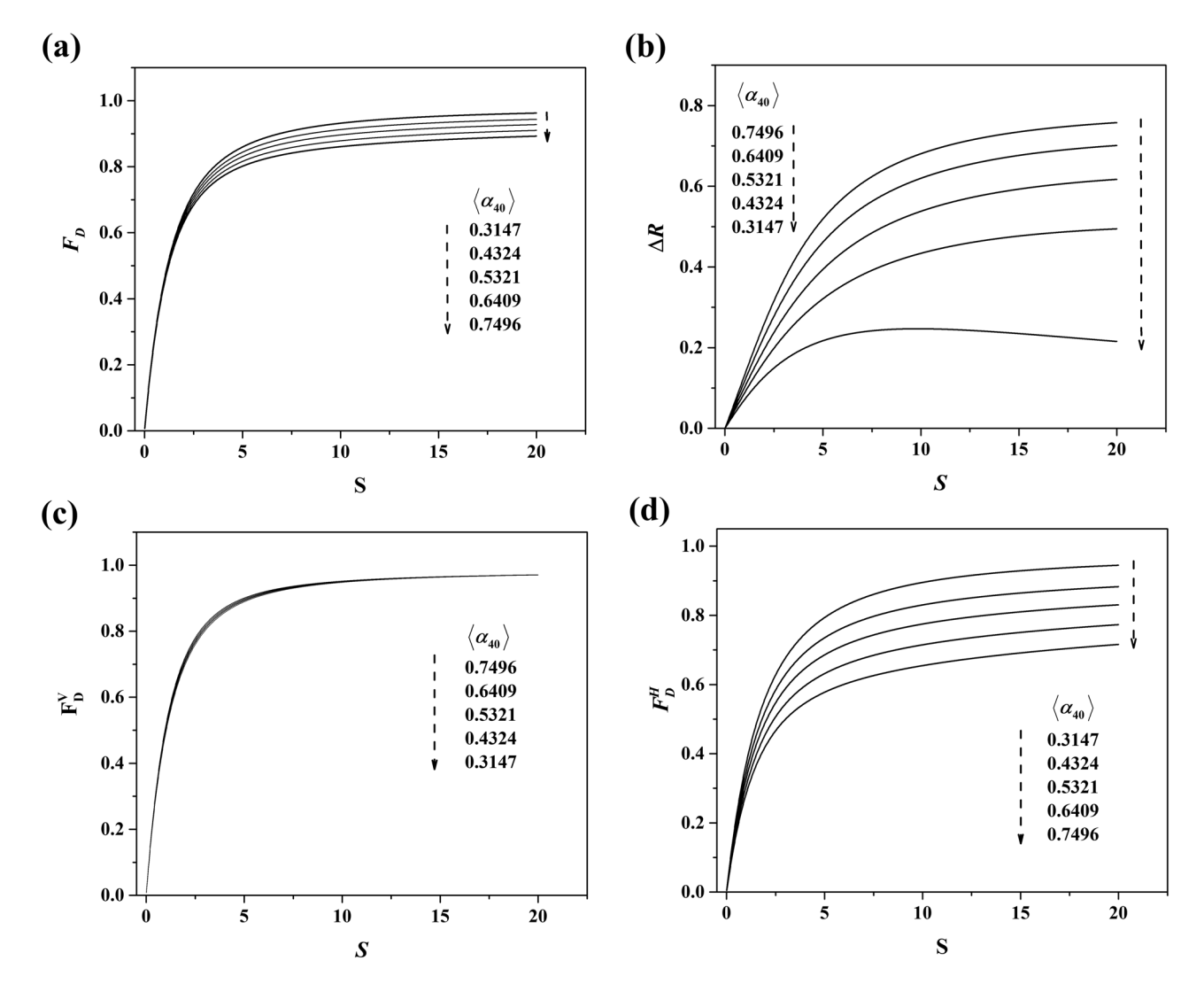


FIG. 5. A simulation of the dependence of STED fluorescence observables on the degree of initial hexadecapolar (K = 4) alignment with $t_D/t_{VIB} = 7$ and an initial quadrupolar alignment $\langle \alpha_{20}(0) \rangle / \sqrt{5} = 0.54$.

moment orientations that are initially removed as the dump pulse is applied.

F. STED sensitivity to hexadecapolar alignment

The form of the STED induced intensity and anisotropy changes also depends on the degrees of quadrupolar and hexadecapolar alignment. Whilst $\langle \alpha_{20} \rangle$ can be directly determined from the fluorescence anisotropy, we have recently shown that an initial value for $\langle \alpha_{40} \rangle$ can be predicted based on the structure of the two-photon transition tensor determined by polarized two-photon absorption and fluorescence anisotropy measurements.²⁵ As discussed above, a direct measurement of $\langle \alpha_{40} \rangle$ is not possible via spontaneous emission and can only enter into fluorescence observables by a nonlinear interaction such as STED. In order to determine the initial value and evolution of $\langle \alpha_{40} \rangle$, we need to ascertain the experimental conditions under which changes in $\langle \alpha_{40} \rangle$ are most readily detected. To this end, we conducted simulations of the four STED observables for conditions similar to those for EGFP with $\langle \alpha_{40} \rangle$ as the only variable parameter. The results are shown in Fig. 5. It is clear that F_D^V [Fig. 5(c)] shows negligible $\langle \alpha_{40} \rangle$ dependence at low and high values of S with a very slight variation in the turn over region (values of S ca. 2–6) between (approximately) linear and saturated behavior. The initial distribution chosen for the five simulations corresponded to an initial anisotropy of 0.54 with initial values of $\langle \alpha_{40} \rangle$ within the boundaries for a physically reasonable excited state distribution $[P_{EX}(x) \ge 0]$, characterized solely by $\langle \alpha_{20} \rangle$ and $\langle \alpha_{40} \rangle$ moments. With increasing $\langle \alpha_{40} \rangle$ in the high S limit, F_D^H and F_D are reduced, whilst the degree of STED depolarization ΔR increases. From Fig. 2, it can be seen that the measurement of F_D^H has a considerably lower degree of experimental uncertainty than ΔR and, given the prior determination of t_D/t_{VIB} , from F_D^V and knowledge of $R(\Delta t)$, analysis of F_D^H data using the theory developed above should in the first instance provide the most accurate means of determining $\langle \alpha_{40} \rangle$. Measurement and analysis of $I_V(t)$ and $I_H(t)$ are also independent of any experimental g-factor^{86,87} arising from a polarization bias in fluorescence detection or (small) differences in the collection times of the two datasets.

III. METHODS AND ANALYSIS

A. Experimental procedure

The experimental apparatus utilised to measure STED dynamics for EGFP is illustrated in Fig. 6. The sample, a 40 μ M solution of recombinant EGFP in phosphate buffered saline (PBS), was contained in a 45 μ l quartz cuvette (Hellma) with three optical windows. Two-photon excited stimulated depletion of EGFP was achieved using a regeneratively amplified Ti:sapphire laser (Coherent Mira 900F, Coherent RegA 9000) and an optical parametric amplifier (OPA, Coherent 9400), respectively. The regenerative amplifier produced 140 fs (FWHM) pulses at 800 nm with around 3.2 μ J energy at a repetition rate of 250 kHz. A small portion of this was used for the two-photon excitation of EGFP (approximately 55 nJ on-sample pulse energy) with the remaining output pumping the

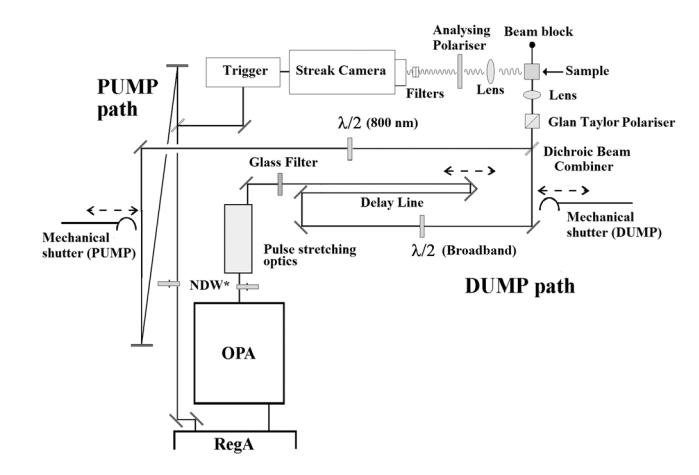


FIG. 6. Schematic diagram of the layout of the STED depletion optics.

OPA which produced 200 fs pulses tuneable between 500 and 700 nm with pulse energies in the region of 300 nJ. The OPA output was temporally stretched using either a TeO₂ crystal (Coherent/Gooch & Housego) to 1.43 ± 0.02 ps (FWHM) in STED cross section measurements or via a holographic grating pair (2400 grooves/mm, Optometrics LLC) to around 5 ps in the determination of $\langle \alpha_{40} \rangle$. Pulse stretching was necessary to both maximise STED efficiency and minimise dump induced two-photon fluorescence. These considerations, together with the onset of dump-induced single photon excitation of EGFP, limited the usable dump wavelength range to between 561 nm and 626 nm. An increase in the dump pulse width to 5 ps minimised the t_D/t_{VIB} dependence of the fluorescence depletion observables making changes to the depletion dynamics brought about by the evolution of $\langle \alpha_{40} \rangle$ more apparent.

Both pump and dump pulse widths (FWHM) were measured with a PulseCheck autocorrelator (APE). In order to ensure that no white light or blue edge remnants remained in the dump pulses, a long pass glass filter was placed in the dump beam prior to recombination with the pump. The two beams were overlapped using a broadband dichroic beam combiner (CVI Optics), passed through a Glan Taylor linear polarizer and a 2.2 mm aperture, and focussed in to the sample with a 2.5 cm achromatic doublet lens (Melles-Griot). The delay between the two beams was adjustable by means of a computer-controlled variable optical delay line (Time and Precision). The pump and dump pulse energies were controlled by means of neutral density wheels and measured with a power meter (Anritsu). Fluorescence was collected in a 90° geometry (see Fig. 1) with a 6.3 cm lens (Melles-Griot), passed through a rotatable polaroid sheet polarizer (Melles-Griot) and focussed onto the entrance slit of the streak camera (Hamamatsu Streak Scope C4334). Any scattered laser light was blocked using appropriate short-pass filters (Corion) and glass infrared cut-off filters (Schott BG39). Consecutive acquisitions of vertically and horizontally polarized emission (see Fig. 1) were obtained and stored on a desktop computer. The dump induced background was subtracted from each signal before construction of the total intensity and anisotropy from the

B. STED data analysis

Development of the protocols for analyzing the depletion data for cross section and ground state relaxation measurement and for determining the evolution of $\langle \alpha_{40} \rangle$ follows the arguments set out in Sec. II C and is further detailed alongside their results in Sec. IV. All approaches involved the modeling of depletion curves using Eqs. (34)–(37), inputting $\langle \alpha_{20}(\Delta t) \rangle$ and $\langle \alpha_{40}(\Delta t) \rangle$, which characterise $P_{EX}(x,\Delta t)$, and t_D/t_{VIB} which, in turn, governs G_{DUMP} . In addition, it is necessary to determine the scaling parameter S_P which connects the dump pulse energy (E_{DUMP}) to the saturation parameter S (see Sec IV B). The pre-dump orientational distribution at time Δt following excitation can be calculated from Eq. (13),

giving

$$P_{EX}(x, \Delta t) = \frac{1}{2} \begin{bmatrix} 1 + \frac{5}{2} [0.54] \exp\left(-\frac{\Delta t (ns)}{17.3}\right) (3x^2 - 1) \\ + \langle \alpha_{40} (\Delta t) \rangle \frac{3}{8} (35x^4 - 30x^2 + 3) \end{bmatrix},$$
(38)

where 0.54 is the measured initial anisotropy in the absence of the dump pulse and 17.3 ns is the corresponding decay time (see Sec. IV A). In the case of F_D^V measurements where the variation in $\langle \alpha_{40}(\Delta t) \rangle$ (across its physically allowable range of values) makes a negligible contribution to the depletion curve, we can safely approximate the un-dumped orientational distribution by

$$P_{EX}(x, \Delta t) = \frac{1}{2} \begin{bmatrix} 1 + \frac{5}{2} [0.54] \exp\left(-\frac{\Delta t (\text{ns})}{17.3}\right) (3x^2 - 1) \\ + [0.381] \exp\left(-\frac{\Delta t (\text{ns})}{0.3 \times 17.3}\right) \frac{3}{8} (35x^4 - 30x^2 + 3) \end{bmatrix},$$
(39)

where 0.381 is the predicted value for $\langle \alpha_{40}(0) \rangle$ based on the two-photon polarization measurements performed previously, ²⁵ and we assume the relationship between τ_{40} and τ_{20} arising from Eq. (9). In generating model curves to fit to F_D^H , $\langle \alpha_{40}(\Delta t) \rangle$ becomes a fitting parameter in its own right,

$$P_{EX}(x, \Delta t) = \frac{1}{2} \left[1 + \frac{5}{2} [0.54] \exp\left(-\frac{\Delta t (\text{ns})}{17.3}\right) (3x^2 - 1) + \langle \alpha_{40} (\Delta t) \rangle \frac{3}{8} (35x^4 - 30x^2 + 3) \right].$$
(40)

Equations (34)–(37) do not have a simple analytical form and require integration over x ($\cos\theta$) for each data point and cannot be used with conventional analysis programmes, in which the fitting parameters are automatically adjusted to find the best fit. It was therefore necessary to implement custom-written software for this task. Model saturation curves were generated using Mathematica (Wolfram Research). For any given combination of Δt , S_P , $\langle \alpha_{40}(\Delta t) \rangle$, and t_D/t_{VIB} , model data points were calculated for $S = E_{DUMP}/S_P$. Custom written Python scripts performed least-squares fitting of the model curves to the experimental data. S_P was fitted in steps of 0.01, t_D/t_{VIB} in steps of 0.25, and $\langle \alpha_{40}(\Delta t) \rangle$ in steps of 0.05. The best fitting curves were judged as those that minimised the sum of the residuals weighted by the experimental uncertainties on the data points.

IV. RESULTS

A. Fluorescence measurements and homo-FRET

The streak camera measurements performed here required an EGFP concentration of 40 μ M to provide sufficient signals, causing homo-FRET to have a noticeable effect on

the fluorescence anisotropy decay. As the undumped fluorescence anisotropy is an important input parameter to the analysis of experimental data, its accurate determination is necessary. Fluorescence anisotropy decays within a 4 ns time window were recorded, all well described by single exponential decay dynamics. An average of eight measurements yielded an initial fluorescence anisotropy of 0.54 ± 0.1 and a decay time of 17.3 ± 0.9 ns. Whilst the initial anisotropy is close to that measured for EGFP at low concentrations (0.552), the fluorescence anisotropy decay at 1 μ M is slower at 19.5 ± 0.10 ns. Theoretical treatments of time dependent fluorescence depolarization due to resonance energy transfer (homo-FRET) in the presence of molecular rotation have been advanced by a number of groups. 80,88 For EGFP where the intrinsic rate of rotational depolarization is slow, the fluorescence anisotropy has been successfully modelled by⁸¹

$$R(t) = R(0) \exp(-t/\tau_{20}) \exp\left(-C\frac{R_0^3}{375}(t/\tau_F)^{1/2}\right).$$
 (41)

Here C is the concentration (in mM) of EGFP and R_0 is the Förster radius (in nm) for homo-transfer. Simulations of the fluorescence decays and the resulting fluorescence anisotropy decay arising from homo-FRET were undertaken as follows. The intrinsic decay parameters were the average fluorescence lifetime of EGFP of 2.75 ns, 26 an intrinsic correlation time τ_{20} of 19.5 ns, $R_0 = 4.65$ nm, 89 and an initial fluorescence anisotropy of 0.552. $I_V(t)$ and $I_H(t)$ were simulated independently using MATLAB (The Mathworks), with a peak channel photon count $[I_V(0) + 2I_H(0)]$ set at 50 000. Poisson noise was added to the two decays separately using the MATLAB poissrnd() function. Intensity and anisotropy decay curves were constructed from $I_V(t)$ and $I_H(t)$ in the usual way (see Fig. 1) and analyzed using a weighted least squares fit (MATLAB)

with the following weighting factors:⁹⁰

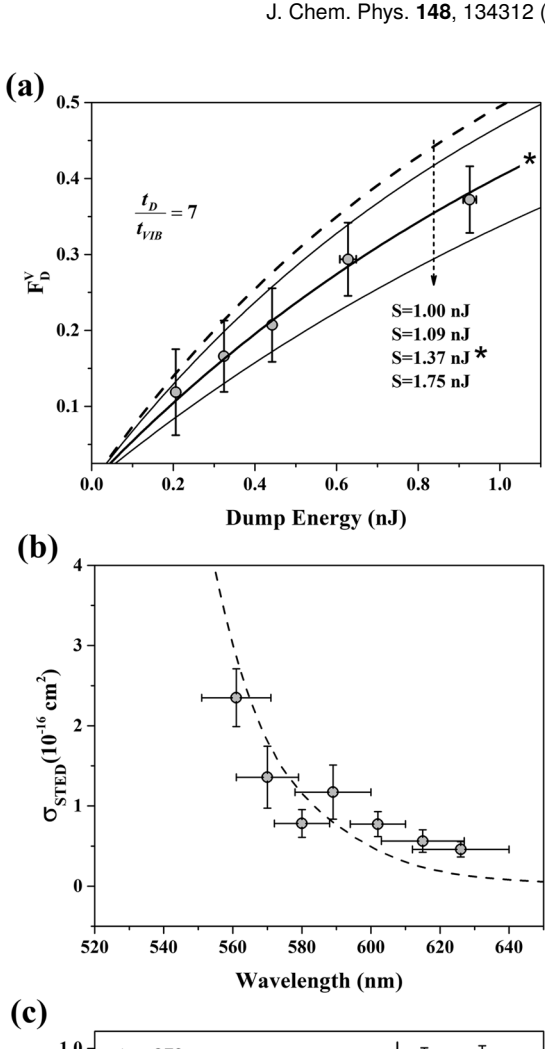
$$\frac{1}{\sigma_I^2} = \frac{1}{I_V + 4I_H},$$

$$\frac{1}{\sigma_P^2} = \frac{I^2}{(I_V + 4I_H)R^2 - 2(I_V - 2I_H)R + I_V + I_H}.$$
(42)

100 simulated datasets were generated, and the mean and standard deviation of the fit parameters were recorded. For an EGFP concentration of 40 μ M, the simulated anisotropy decay was found to be well described by a single exponential correlation time of 18.91 \pm 0.30 ns with $R(0) = 0.548 \pm 0.001$. By contrast, the measured decays, whilst yielding a comparable initial anisotropy (0.54 \pm 0.01), had a shorter correlation time of 17.3 \pm 0.9 ns. Previous work⁸¹ had suggested that R_0 for EGFP may be significantly higher than 4.65 nm which would indeed result in a further reduction in the anisotropy decay time. To investigate this possibility, we generated a set of simulated anisotropy decays for EGFP at 40 μ M with R_0 values from 1 nm to 10 nm. A second order polynomial fit to the data points indicates that the 40 μ M correlation time of 17.3 \pm 0.9 ns corresponds to $R_0 = 7 \pm 1$ nm, comparable with the value of 7.3 ± 0.1 nm reported from concentration dependent frequency domain fluorescence anisotropy measurements.⁸¹ Homo-FRET is thus an active depolarization mechanism for the quadrupolar transition dipole moment alignment and, in addition to molecular rotation, can also be expected to influence the relaxation of the hexadecapolar alignment prepared by two-photon excitation.

B. STED cross section and ground state relaxation measurements

Maximum time-resolution (15 ps) was achieved by using a 2 ns time measurement window. The pump-dump delay was set to 373 ps for all experiments. The dump wavelength was varied between 561 and 626 nm, 561 nm being the threshold wavelength below which the degree of dump-induced fluorescence from the unexcited EGFP population (approximately 99.7% of the total number of EGFP molecules in the excitation-detection volume) precluded accurate measurements. For each dump wavelength, the pulse energy was varied from approximately $0.5 \,\mathrm{nJ}$ to $50 \,\mathrm{nJ}$. F_D^V values at each dump energy were determined by the calculation of the fractional loss of V-polarized fluorescence intensity after application of the dump pulse relative to an experiment in which no dump was applied. The intensity values just after the dump pulse were calculated by taking an average over 50 channels (0.208 ns) following completion of the dump (defined as the first channel to show an upward fluctuation in intensity or anisotropy following the rapid loss). Given the long rotational diffusion time of EGFP (17.3 ns), this did not result in a significant error in the anisotropy change. From Fig. 5(c), it can be seen that the $\langle \alpha_{40} \rangle$ dependence on F_D^V is minimal. For cross section determination, the fitting process was therefore concerned with finding a best fitting combination of S_P and t_D/t_{VIB} based only upon the use of the F_D^V data. From the model saturation curves of Fig. 4, it can be seen that in the region where the variation of F_D^V with S is approximately linear, the dependence of F_D^V on t_D/t_{VIB} is minimal. The representative data plotted in Fig. 7 were obtained for a dump wavelength of



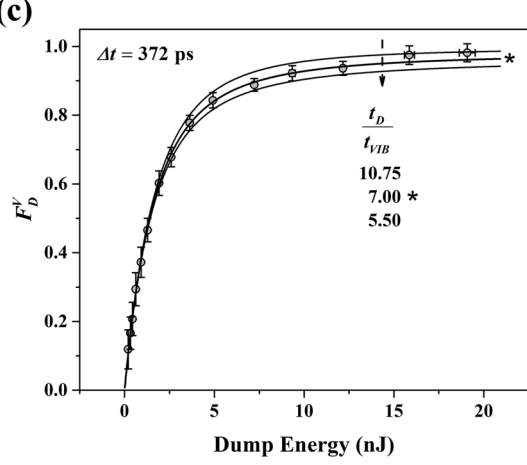


FIG. 7. Cross section and lower level relaxation time measurement. (a) Low energy portion of the F_D^V depletion curve (t_D/t_{VIB} sensitivity minimized) showing the best (nonlinear least squares fit) scaled depletion curve $(S_P = 1.37)$. The uncertainty in S_P was determined by the best fits to the upper and lower experimental error bars ($S_P = 1.75$ and 1.09, respectively). (b) A plot of the measured cross section as a function of dump wavelength superimposed on the relative fluorescence intensity of EGFP (dashed line). (c) Calculation of t_D/t_{VIB} was determined by a full fit to the depletion data [using $S_P = 1.37$ determined in (a)] yielding $t_D/t_{VIB} = 7$.

570 nm. Taking an estimate for $t_D/t_{VIB} = 7$, a model depletion curve was generated for F_D^V using Eq. (28), inputting values of the un-dumped anisotropy calculated from the measured decay data [R(0) and τ_{20}], $\langle \alpha_{40}(0) \rangle = 0.381$ from our companion paper²⁵ and a depolarization time of $0.3\tau_{20}$ [Eq. (7)]. This is overlaid with the experimental data [dashed line in Fig. 7(a)],

TABLE I. Dump wavelength variation in the relaxation times of the upper S_0 vibrational levels accessed by STED.

Dump wavelength (nm)	$ au_{DUMP}$ (ps)	$\tau_{\it VIB}$ (fs)	
561	1.24 ± 0.04	146 ± 86 199 ± 106 219 ± 122 228 ± 97 191 ± 76 223 ± 64	
570	1.39 ± 0.02		
580	1.48 ± 0.08		
589	1.48 ± 0.08		
602	1.43 ± 0.02		
615	1.56 ± 0.07		
626	1.46 ± 0.08	139 ± 119	
Weighted average:		196 ± 34fs	

in which S is equivalent to E_D (in nJ). A series of these (otherwise identical) F_D^V plots were generated, in which S_P was varied until a best fit to the experimental data was achieved.

In Fig. 7(a), this plot is denoted by an asterisk and corresponds to $S_P = 1.37$. The STED cross section is then calculated from

$$\sigma_{STED} = \frac{Ah\nu_{DUMP}}{S_P \times 10^{-9}}. (43)$$

Values for the cross sectional area A at each dump wavelength were calculated assuming Gaussian focusing of the dump beam⁹¹

$$A_{\lambda} = \frac{4}{\pi} \left(\frac{\lambda f}{D}\right)^2,\tag{44}$$

where D is the input spot size (2.2 mm) and f is the focal length (25 mm), giving values for A varying between 5.2×10^{-7} cm² and 6.4×10^{-7} cm². A plot of the variation in σ_{STED} with dump wavelength is shown in Fig. 7(b). Analysis of the full range of the experimental data is obtained by

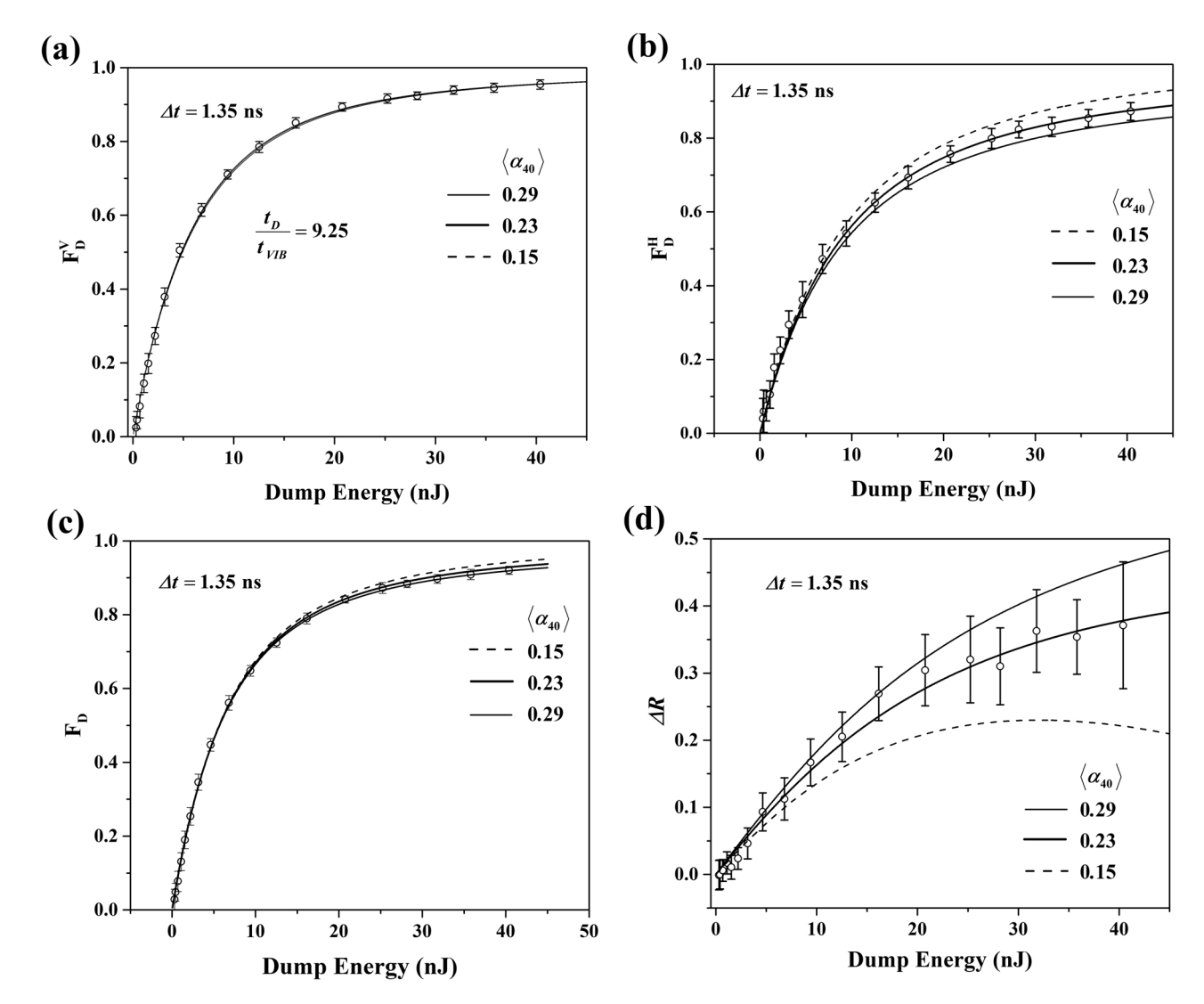
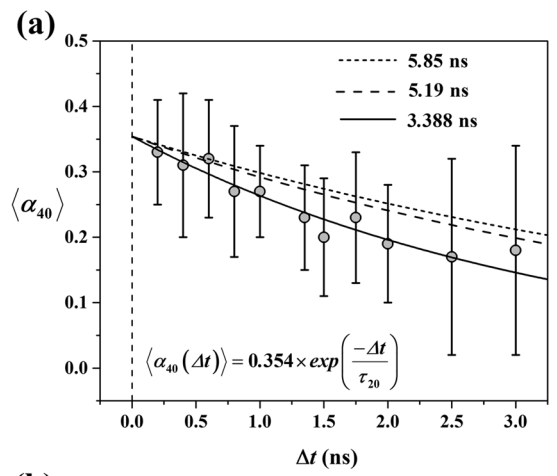
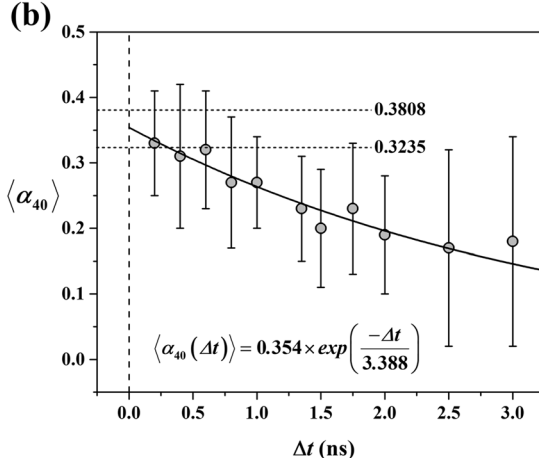


FIG. 8. Analysis of F_D^V , F_D^H , F_D , and ΔR data for a pump-dump delay of 1.35 ns. (a) Fits to F_D^V are insensitive to $\langle \alpha_{40} \rangle$ and the data are best fit by t_D/t_{VIB} = 9.25. (b) F_D^H analysis: fixing t_D/t_{VIB} at 9.25, the best fit to the data was obtained for $\langle \alpha_{40} \rangle = 0.23$. In Method I, the uncertainty in $\langle \alpha_{40} \rangle$ was determined by the (computer generated) best fit to the upper and lower error bars, yielding a maximum uncertainty of ± 0.08 . [(c) and (d)] Model curves based on the fitting parameters in (a) and (b) are drawn through the data. It can be seen that the value of the lower bound to $\langle \alpha_{40} \rangle$ (dashed line) is too low. In Method II, the best fit of model curves to the error bars was judged by eye. This yields an uncertainty in $\langle \alpha_{40} \rangle$ of ± 0.05 .

generating model F_D^V plots (as above) with a range of t_D/t_{VIB} values. The best fit to the experimental data points and their associated uncertainties were combined with the





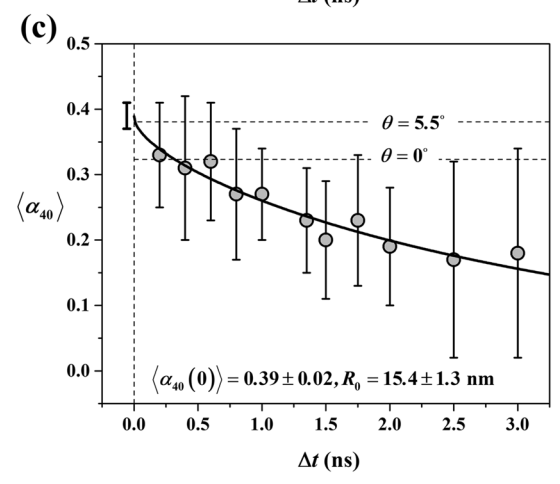


FIG. 9. Plots of the variation in the degree of hexadecapolar alignment as a function of pump-dump delay. (a) shows a single exponential fit to the data yielding a time zero value of 0.351 ± 0.012 and a correlation time of 3.388 ± 0.357 ns. The dashed lines show previously predicted $\langle \alpha_{40}(0) \rangle$ values for emission transition dipole moments oriented at angles of 5.5° and 0° to the principal axis of the two photon transition tensor. (b) shows a comparison between the fitted single exponential decay and the hexadecapolar alignment decay predicted for pure rotational diffusion at $1~\mu$ M (5.67 ns) and assuming the relationship between the measured anisotropy decay time and τ_{40} is applicable in the presence of FRET at $40~\mu$ M (5.19 ns). (c) shows a least squares fit of Eq. (41) to the data with $\tau_{20} = 19.5$ ns. This yields $\langle \alpha_{40}(0) \rangle = 0.39 \pm 0.02$ and $R_0(K=4) = 15.5 \pm 1.3$ nm. The vertical line indicates the uncertainty in $\langle \alpha_{40}(0) \rangle$.

measured pulsewidth (autocorrelation FWHM/ $\sqrt{2}$) [Fig. 7(c)], from which t_{VIB} can be determined (see Table I).

C. Hexadecapolar alignment dynamics

As can be seen from the model plots in Figs. 4 and 5, both t_D/t_{VIB} and $\langle \alpha_{40} \rangle$ act to reduce F_D and ΔR in the saturation region. As discussed above, the best strategy to differentiate between the two quantities and determine the time evolution $\langle \alpha_{40} \rangle$ was first to analyze F_D^V (which shows a minimal $\langle \alpha_{40} \rangle$ dependence) to obtain t_D/t_{VIB} , and then with this information proceed to analyze the corresponding F_D^H data to obtain $\langle \alpha_{40} \rangle$. In order to minimise the dependence of the STED observables on t_D/t_{VIB} , the dump pulse (typically 600-607 nm with a spectral FWHM of 12-15 nm) was stretched using a grating pair to produce a temporal FWHM of at least 5 ps. F_D^V , F_D^H , F_D , and ΔR saturation curves were recorded for pump-dump delays Δt ranging from 200 ps to 3 ns.

Figure 8 shows representative data and analysis for a pump-dump delay of 1.35 ns, yielding a value for $\langle \alpha_{40} \rangle$ of 0.23 \pm 0.06. A plot of the variation of $\langle \alpha_{40} \rangle$ with Δt is shown in Fig. 9. The data can be fitted by an exponential decay corresponding to an initial (pre-dump) value of 0.354 \pm 0.012 and a decay time of 3.39 \pm 0.36 ns (R² = 0.91).

V. DISCUSSION

At all dump wavelengths, the degree of (saturated) depletion in the polarized intensity and total fluorescence was high, varying from close to 100% at 561 nm to 90% at 626 nm. We have previously observed that the fluorescence decay dynamics of recombinant EGFP are well described by a bi-exponential decay, 25,26 corresponding to two distinct and approximately equally weighted excited state populations. In recent work, one of these was found to be wholly inactive in FRET to mCherry arising from the homodimerisation of PDK1.²⁶ As the emission from mCherry is also bi-exponential, four FRET pathways should have been active. However, only one (to the minority mCherry decay component) was observed. Two potential mechanisms for this restriction were proposed, the first based on local transition dipole moment orientations with one population FRET inactive due to a low κ^2 factor⁹² and the second arising from a disparity in emission transition dipole moment strengths. The latter mechanism, if present, would reduce the degree of depletion attainable which is clearly not the case. This mechanism can therefore be discounted. This conclusion is born out by recent work investigating FRET to mCherry, in which EGFP was replaced by Oregon Green, a more mobile and homogeneous (single lifetime) donor but with similar spectral properties to EGFP. No restrictions were observed, indicating that the increase in the local orientational freedom of the donor gave rise to unrestricted

The STED cross section values obtained range from 4.59×10^{-17} cm² (626 nm) to 2.35×10^{-16} cm² (561 nm). The wavelength dependence of σ_{STED} follows the rise in the spontaneous emission spectrum with decreasing wavelength [dashed line in Fig. 7(b)]. The values obtained are comparable in magnitude to previous measurements on EGFP (520-570 nm).⁹³ From Table I, it can be seen that the ground

state relaxation time remains approximately constant across the spectrum with a weighted mean of 196 \pm 34 fs. As the dump wavelength decreases, the vibrational states accessed by stimulated emission will be energetically closer to the thermal equilibrium distribution, and thus τ_{VIB} (the inverse of the relaxation rate) would be expected to increase. This was not observed, indicating that stimulated emission is highly efficient across this part of the spectrum. The H-bonding network surrounding the EGFP chromophore 94,95 (which restricts conformational flexibility) may act to assist ground-state relaxation through the provision of a high density of states for intra-molecular vibrational coupling. 96,97 STED in EGFP is highly efficient and, in spite of a rapidly relaxing excited state ($\langle \tau \rangle = 2.75$ ns), the sub-picosecond ground state vibrational relaxation provides the basis for an efficient 4-level laser which has been demonstrated in solution, crystals, and live cells.98-100

The hexadecapolar alignment measurements yielded values for $\langle \alpha_{40} \rangle$ for pump probe delay times spanning 200 ps to 3 ns, as displayed in Fig. 9. The measurement of STED observables at pump-dump delays closer to $\Delta t = 0$ was precluded by the need to determine an accurate value for the pre-dump intensity so that the degree of depletion could be determined with a minimal degree of uncertainty. If the hexadecapolar alignment dynamics in EGFP are well described by a single exponential decay, then extrapolation to $\Delta t = 0$ yields a value for the initial hexadecapolar alignment of 0.354 ± 0.012 [see Fig. 9(a)], larger than the value of 0.3235 calculated for a transition dipole moment angle of 0° but closer to that of 0.381 calculated for a transition dipole moment angle of 5.5°. 25 Like the quadrupolar alignment dynamics (directly measured by the fluorescence anisotropy), the hexadecapolar transition dipole alignment will be altered by homo-FRET as well as rotational diffusion. The decay of $\langle \alpha_{40} \rangle$ in the case of pure rotational diffusion (given a rotational diffusion time of 19.5 ns) from Eq. (9) should be characterised by an exponential lifetime of 5.85 ns. If we were to assume that this relationship holds in the presence of homo-FRET, the hexadecapolar alignment should be characterised by an exponential lifetime of 5.19 ns ($\tau_{20} = 17.3$ ns). These two decays are plotted in Fig. 9(c), and it is clear that the hexadecapolar relaxation dynamics are considerably faster. The form of hexadecapolar dipole relaxation in the presence of homo-FRET has yet to be derived theoretically. With the assumption that, as in Eq. (41), the overall correlation function can be described by the product of the correlation function for rotational diffusion together with that for energy migration,⁸¹ the hexadecapolar dipole alignment dynamics would take the form

$$\langle \alpha_{40} (\Delta t) \rangle = \langle \alpha_{40} (\Delta t = 0) \rangle \exp(-10t/3\tau_{20})$$

$$\times \exp\left(-C \frac{R_0 (K = 4)^3}{375} (t/\tau_F)^{1/2}\right), \quad (45)$$

where $R_0(K=4)$ corresponds to the apparent Förster radius for hexadecapolar depolarization. A least squares fit to the data taking $\tau_{20}=19.5$ ns and $\tau_F=2.75$ ns yields an initial value for $\langle \alpha_{40}(0) \rangle$ of 0.39 ± 0.2 and a value for $R_0(K=4)$ of 15 ± 1 nm. The increase in the apparent Förster radius for homo-FRET over the value of 7 nm obtained above and

TABLE II. Least squares fitting results of Eq. (41) to the STED measurements of the hexadecapolar alignment evolution in EFGP shown in Fig. 9. In Method I, the uncertainties in $\langle \alpha_{40}(\varDelta t) \rangle$ are calculated by a least squares fits of the model decay curves to the upper and lower bounds of the experimental error bars in the F_D^H data. In Method II, the upper and lower values of $\langle \alpha_{40}(\varDelta t) \rangle$ are determined by inspection of model curves across F_D^H , F_D , and $\varDelta R$.

Method	I	II	I	II
$\langle \alpha_{40} (0) \rangle$	0.39 ± 0.02	0.40 ± 0.03	0.3808 (fixed)	0.3808 (fixed)
$R_0(K = 4) \text{ nm}$	15.4 ± 1.3	16.1 ± 1.4	15.0 ± 0.5	15.1 ± 0.5

in previous work⁸¹ for fluorescence depolarization is a necessary consequence arising from the need to account for the increased degree of homo-FRET depolarization in $\langle \alpha_{40}(\Delta t) \rangle$, as is evident from Fig. 9(b). Setting $\langle \alpha_{40}(0) \rangle$ at 0.381 as we previously predicted for an emission dipole moment direction of 5.5° relative to the transition tensor axis²⁵ yields a similar value for $R_0(K=4)$ of 15.0 \pm 0.5 nm. These results, together with an alternative approach to the determination in the uncertainties in the $\langle \alpha_{40}(\Delta t) \rangle$ measurements, are summarised in Table II.

VI. CONCLUSIONS

We have shown that STED is able to equally depopulate the sub-populations that make up the fluorescence emission in EGFP, further reinforcing the conclusions of recent work³² which indicated that restrictions in fluorescent protein FRET arise from local orientational constraints rather than a difference in intrinsic transition dipole moment strengths. STED in EGFP was found to be efficient, aided by a short lifetime (approximately 194 fs) for the ground state vibrational levels which minimises the degree of excited state re-pumping as the dump pulse energy is increased.

Theoretical modelling has shown the importance of performing polarization-resolved STED measurements in extracting meaningful data, exemplified by the relative sensitivities of F_D^V and F_D^H to changes in the hexadecapolar alignment created by two-photon absorption. The hexadecapolar alignment yields important information, first in terms of determining the structure of the two-photon transition tensor in EGFP and the direction of the emission transition dipole moment in the molecular frame. The initial value of $\langle \alpha_{40} \rangle$ corresponds to that predicted by linear and circularly polarized two-photon fluorescence measurements for a planar transition and near-diagonal tensor with an emission transition dipole moment orientation of 5.5° to the principal axis. 25

The hexadecapolar transition dipole alignment dynamics reported are, to the best of our knowledge, the first measurement of higher order (rank K > 2) dipole moment correlations in resonance energy transfer. The increased sensitivity of the hexadecapolar alignment to depolarization over that reported by the fluorescence anisotropy is marked. Our results point to the perhaps not unexpected departure from the small step rotational diffusion relationship that exists between K = 2 and K = 4 dipole relaxation. Modeling the composite fluorescence anisotropy as the product of two independent correlation functions [Eq. (41)] was justified based on the slow (19.5 ns)

rotational correlation time of EGFP.⁸¹ For K = 4 rotational diffusion in EGFP, this time is considerably shorter (5.85 ns) and it may be that this approximation no longer holds. As far as we are aware, the form of the K = 4 homo-FRET decay has yet to be investigated. We hope that this work will provide an impetus for such studies. We anticipate that the ability to probe higher order dipole alignment transfer in hetero-FRET would also provide a useful adjunct to current time-resolved polarization techniques^{26,32} yielding additional information and providing a clearer insight into molecular orientation, interactions, and resonance energy transfer.

ACKNOWLEDGMENTS

We are grateful to the Engineering & Physical Sciences Research Council for financial support of this work through Ph.D. studentships awarded to T.A.M. and T.S.B. via the CoMPLEX doctoral training centre at UCL. We would like to thank Sara Kisakye-Nambozo and Svend Kjaer (Cancer Research UK, Lincoln's Inn Fields) for their help in the preparation and purification of recombinant EGFP.

APPENDIX: DEFINITE GAUSSIAN INTEGRALS

$$A_{0} = \int_{-1}^{1} \exp\left(-Sx^{2}\right) dx = \frac{\sqrt{\pi}erf\left(\sqrt{S}\right)}{\sqrt{S}},$$

$$A_{2} = \int_{-1}^{1} x^{2} \exp\left(-Sx^{2}\right) dx = \frac{\sqrt{\pi}erf\left(\sqrt{S}\right)}{2S^{3/2}} - \frac{\exp\left(-S\right)}{S},$$

$$A_{4} = \int_{-1}^{1} x^{4} \exp\left(-Sx^{2}\right) dx = \frac{3\sqrt{\pi}erf\left(\sqrt{S}\right)}{4S^{5/2}} - \frac{(2S+3)\exp\left(-S\right)}{2S^{2}},$$

$$A_{6} = \int_{-1}^{1} x^{6} \exp\left(-Sx^{2}\right) dx = \frac{15\sqrt{\pi}erf\left(\sqrt{S}\right)}{8S^{7/2}}$$

$$-\frac{(2S(2S+5)+15)\exp\left(-S\right)}{4S^{3}}.$$

Integrals calculated using the WolframlAlpha package (Wolfram Research).

- ¹D. E. Reisner, R. W. Field, J. L. Kinsey, and H. Dai, J. Chem. Phys. 80,
- ²I. Gryczynski, J. Kusba, and J. R. Lakowicz, J. Phys. Chem. 98, 8886
- ³J. Kuśba, V. Bogdanov, I. Gryczynski, and J. R. Lakowicz, Biophys. J. **67**, 2024 (1994).
- ⁴Q. Zhong, Z. Wang, Y. Sun, Q. Zhu, and F. Kong, Chem. Phys. Lett. 248,
- 277 (1996). ⁵S. A. Kovalenko, N. P. Ernsting, and J. Ruthmann, J. Chem. Phys. 106,
- 3504 (1997). ⁶G. Haran, E. A. Morlino, J. Matthes, R. H. Callender, and R. M.
- Hochstrasser, J. Phys. Chem. A 103, 2202 (1999). ⁷P. Changenet-Barret, C. T. Choma, E. F. Gooding, W. F. DeGrado, and R.
- M. Hochstrasser, J. Phys. Chem. B 104, 9322 (2000). ⁸C. Buehler, C. Y. Dong, P. T. C. So, T. French, and E. Gratton, Biophys. J. **79**, 536 (2000).
- ⁹T. A. Klar, S. Jakobs, M. Dyba, A. Egner, and S. W. Hell, Proc. Natl. Acad. Sci. U. S. A. 97, 8206 (2000).
- ¹⁰K. I. Willig, B. Harke, R. Medda, and S. W. Hell, Nat. Methods 4, 915 (2007).

- ¹¹B. Huang, M. Bates, and X. Zhuang, Annu. Rev. Biochem. **78**, 993 (2009).
- ¹²G. Vicidomini, G. Moneron, K. Y. Han, V. Westphal, H. Ta, M. Reuss, J. Engelhardt, C. Eggeling, and S. W. Hell, Nat. Methods 8, 571 (2011).
- ¹³T. A. Klar and S. W. Hell, Opt. Lett. **24**, 954 (1999).
- ¹⁴K. I. Willig, R. Kellner, R. Medda, B. Hein, S. Jakobs, and S. W. Hell, Nat. Methods 3, 721 (2006).
- ¹⁵B. R. Rankin, G. Moneron, C. A. Wurm, J. C. Nelson, A. Walter, D. Schwarzer, J. Schroeder, D. A. Colón-Ramos, and S. W. Hell, Biophys. J. 100, L63 (2011).
- ¹⁶R. Marsh, D. Armoogum, and A. Bain, Chem. Phys. Lett. **366**, 398 (2002).
- ¹⁷R. J. Marsh, N. D. Leonczek, D. A. Armoogum, E. M. Monge, and A. J. Bain, Proc. SPIE 5925, 59250C (2005).
- ¹⁸D. A. Armoogum, R. J. Marsh, and A. J. Bain, Proc. SPIE **5222**, 34–44 (2003).
- ¹⁹A. J. Bain, R. J. Marsh, D. A. Armoogum, O. Mongin, L. Porrès, and M. Blanchard-Desce, Biochem. Soc. Trans. 31, 1047 (2003).
- ²⁰R. J. Marsh, N. D. Leonczek, D. A. Armoogum, L. Porres, O. M. Mongin, M. H. Blanchard-Desce, and A. J. Bain, Proc. SPIE 5510, 117 (2004).
- ²¹D. A. Armoogum, R. J. Marsh, N. Nicolaou, O. Mongin, M. Blanchard-Desce, and A. J. Bain, Proc. SPIE 7030, 70300S (2008).
- ²²S.-Y. Chen and B. W. Van Der Meer, Biophys. J. **64**, 1567 (1993).
- ²³P. R. Callis, J. Chem. Phys. **99**, 27 (1993).
- ²⁴C. Wan and C. K. Johnson, Chem. Phys. **179**, 513 (1994).
- ²⁵T. A. Masters, R. J. Marsh, T. S. Blacker, D. A. Armoogum, B. Larijani, and A. J. Bain, J. Chem. Phys. 148, 134311 (2018).
- ²⁶T. A. Masters, R. J. Marsh, D. A. Armoogum, N. Nicolaou, B. B. Larijani, and A. J. Bain, J. Am. Chem. Soc. 135, 7883 (2013).
- ²⁷T. A. Masters, V. Calleja, D. A. Armoogum, R. J. Marsh, C. J. Applebee, M. Laguerre, A. J. Bain, and B. Larijani, Sci. Signaling 3, ra78 (2010).
- ²⁸ A. A. Heikal, S. T. Hess, and W. W. Webb, Chem. Phys. **274**, 37 (2001).
- ²⁹S. T. Hess, E. D. Sheets, A. Wagenknecht-Wiesner, and A. A. Heikal, Biophys. J. 85, 2566 (2003).
- ³⁰A. J. W. G. Visser, S. P. Laptenok, N. V Visser, A. van Hoek, D. J. S. Birch, J.-C. Brochon, and J. W. Borst, Eur. Biophys. J. 39, 241 (2010).
- ³¹D. L. Andrews and A. A. Demidov, Resonance Energy Transfer (Wiley, 1999).
- ³²T. S. Blacker, W. Y. Chen, E. Avezov, R. J. Marsh, M. R. Duchen, C. F. Kaminski, and A. J. Bain, J. Phys. Chem. C 121, 1507 (2017).
- ³³A. J. Bain and A. J. McCaffery, Chem. Phys. Lett. **108**, 275 (1984).
- ³⁴A. J. Bain and A. J. McCaffery, J. Chem. Phys. 83, 2641 (1985).
- ³⁵A. J. Bain, *Photonics* (John Wiley & Sons, Inc., Hoboken, NJ, USA, 2015), pp. 279–320.

 ³⁶ A. J. Bain, P. Chandna, and J. Bryant, J. Chem. Phys. **112**, 10418 (2000).
- ³⁷A. J. Bain, An Introduction to Laser Spectroscopy (Springer US, Boston, MA, 2002), pp. 171-210.
- ³⁸E. M. Monge, D. A. Armoogum, and A. J. Bain, Proc. SPIE **4797**, 264–274
- ³⁹A. J. Bain and A. J. McCaffery, J. Chem. Phys. **83**, 2627 (1985).
- ⁴⁰C. H. Greene and R. N. Zare, Annu. Rev. Phys. Chem. **33**, 119 (1982).
- ⁴¹C. H. Greene and R. N. Zare, J. Chem. Phys. **78**, 6741 (1983).
- ⁴²P. Ferrand, P. Gasecka, A. Kress, X. Wang, F.-Z. Bioud, J. Duboisset, and S. Brasselet, Biophys. J. 106, 2330 (2014).
- ⁴³S. D. Durbin and Y. R. Shen, Phys. Rev. A **30**, 1419 (1984).
- ⁴⁴W. A. Wegener, Biophys. J. **46**, 795 (1984).
- ⁴⁵R. Swaminathan, C. Hoang, and A. Verkman, Biophys. J. **72**, 1900
- ⁴⁶M. Bell, R. Dale, U. van der Heide, and Y. Goldman, Biophys. J. **83**, 1050 (2002)
- ⁴⁷M. Velez and D. Axelrod, Biophys. J. **53**, 575 (1988).
- ⁴⁸C. Kuan, H. Mayne, and R. Wolf, Chem. Phys. Lett. **133**, 415 (1987).
- ⁴⁹G. C. Corey and M. H. Alexander, J. Chem. Phys. **87**, 4937 (1987).
- ⁵⁰H. F. Bowen, D. J. Kouri, R. C. Mowrey, A. T. Yinnon, and R. B. Gerber, J. Chem. Phys. 99, 704 (1993).
- ⁵¹A. G. Smolin, O. S. Vasyutinskii, E. R. Wouters, and A. G. Suits, J. Chem. Phys. 121, 6759 (2004).
- ⁵²O. V. Elyukhina, O. S. Vasyutinskii, and J. A. Beswick, Opt. Spectrosc. **94**, 369 (2003).
- ⁵³C. Zannoni, Mol. Phys. **42**, 1303 (1981).
- ⁵⁴M. Van Zandvoort, H. C. Gerritsen, G. Van Ginkel, Y. K. Levine, R. Tarroni, and C. Zannoni, J. Phys. Chem. B 101, 4149 (1997).
- ⁵⁵C. Zannoni, A. Arcioni, and P. Cavatorta, Chem. Phys. Lipids 32, 179
- ⁵⁶W. Li, Y. Wang, H. Shao, Y. He, and H. Ma, Proc. SPIE **6047**, 60472R

- ⁵⁷A. H. Orrego, C. García, J. M. Mancheno, J. M. Guisán, M. P. Lillo, and F. López-Gallego, J. Phys. Chem. B 120, 485 (2016).
- ⁵⁸P. J. W. Debye, *Polar Molecules* (Chemical Catalog Company, Incorporated, 1929).
- ⁵⁹ A. J. Bain, P. Chandna, G. Butcher, and J. Bryant, J. Chem. Phys. 112, 10435 (2000).
- ⁶⁰C. Fiorini, F. Charra, and J.-M. Nunzi, J. Opt. Soc. Am. B 11, 2347 (1994).
- ⁶¹F. Charra, F. Devaux, J.-M. Nunzi, and P. Raimond, Phys. Rev. Lett. 68, 2440 (1992).
- ⁶²C. Fiorini, I. D. W. Samuel, J. Zyss, F. Charra, and J.-M. Nunzi, Opt. Lett. 20, 2469 (1995).
- ⁶³S. Lin, I. D. Hands, D. Andrews, and S. R. Meech, J. Phys. Chem. A 103, 3830 (1999).
- ⁶⁴D. Laage and J. T. Hynes, Science **311**, 832 (2006).
- ⁶⁵E. N. Ivanov, Sov. Phys. JETP **18**, 1041 (1964).
- ⁶⁶G. Williams, Chem. Rev. **72**, 55 (1972).
- ⁶⁷R. G. Gordon, J. Chem. Phys. **43**, 1307 (1965).
- ⁶⁸D. J. Cook, J. X. Chen, E. A. Morlino, and R. M. Hochstrasser, Chem. Phys. Lett. **309**, 221 (1999).
- ⁶⁹A. Arcioni, R. Tarroni, and C. Zannoni, Il Nuovo Cimento D 10, 1409 (1988).
- ⁷⁰A. Arcioni, F. Bertinelli, R. Tarroni, and C. Zannoni, Chem. Phys. **143**, 259 (1990).
- ⁷¹W. Van der Meer, H. Pottel, W. Herreman, M. Ameloot, H. Hendrickx, and H. Schröder, Biophys. J. 46, 515 (1984).
- ⁷²I. Dozov and N. Kirov, J. Chem. Phys. **90**, 1099 (1989).
- ⁷³R. M. Hochstrasser and D. K. Negus, Proc. Natl. Acad. Sci. U. S. A 81, 4399 (1984).
- ⁷⁴T. M. Jovin, D. S. Lidke, and J. N. Post, Proc. SPIE **5323**, 1 (2004).
- ⁷⁵A. L. Mattheyses, A. D. Hoppe, and D. Axelrod, Biophys. J. **87**, 2787 (2004).
- ⁷⁶D. W. Piston and G.-J. Kremers, Trends Biochem. Sci. 32, 407 (2007).
- ⁷⁷P. A. Anfinrud, D. E. Hart, and W. S. Struve, J. Phys. Chem. **92**, 4067 (1988)
- ⁷⁸J. A. Pescatore and I. Yamazaki, J. Phys. Chem. **100**, 13333 (1996).

- ⁷⁹D. E. Hart, P. A. Anfinrud, and W. S. Struve, J. Chem. Phys. **86**, 2689 (1987).
- ⁸⁰S. Engstrom, M. Lindberg, and L. B. Johanssonb, J. Chem. Phys. **96**, 7528 (1992).
- ⁸¹A. H. A. Clayton, Q. S. Hanley, D. J. Arndt-Jovin, V. Subramaniam, and T. M. Jovin, Biophys. J. 83, 1631 (2002).
- ⁸²M. Kasha, Discuss. Faraday Soc. **9**, 14 (1950).
- ⁸³M. Drobizhev, N. S. Makarov, S. E. Tillo, T. E. Hughes, and A. Rebane, Nat. Methods 8, 393 (2011).
- ⁸⁴G. Vicidomini, P. Bianchini, and A. Diaspro, Nat. Methods 15, 173 (2018).
- 85 A. E. Siegman, Lasers (University Science Books, 1986).
- ⁸⁶ A. J. Cross and G. R. Fleming, Biophys. J. **46**, 45 (1984).
- ⁸⁷D. O'Connor, *Time-Correlated Single Photon Counting* (Academic Press, 2012).
- ⁸⁸G. H. Fredrickson, J. Chem. Phys. **88**, 5291 (1988).
- ⁸⁹G. H. Patterson, D. W. Piston, and B. G. Barisas, Anal. Biochem. **284**, 438
- ⁹⁰T. S. Blacker, R. J. Marsh, M. R. Duchen, and A. J. Bain, Chem. Phys. **422**, 184 (2013).
- ⁹¹O. Svelto and D. C. Hanna, *Principles of Lasers* (Springer, 1998).
- ⁹²R. E. Dale and J. Eisinger, Biopolymers **13**, 1573 (1974).
- ⁹³E. Rittweger, B. R. Rankin, V. Westphal, and S. W. Hell, Chem. Phys. Lett. 442, 483 (2007).
- ⁹⁴J. A. J. Arpino, P. J. Rizkallah, and D. D. Jones, PLoS One 7, e47132 (2012).
- ⁹⁵A. Royant and M. Noirclerc-Savoye, J. Struct. Biol. **174**, 385 (2011).
- ⁹⁶T. Elsaesser and W. Kaiser, Annu. Rev. Phys. Chem. **42**, 83 (1991).
- ⁹⁷M. Silva, R. Jongma, R. W. Field, and A. M. Wodtke, Annu. Rev. Phys. Chem. **52**, 811 (2001).
- ⁹⁸C. P. Dietrich, A. Steude, L. Tropf, M. Schubert, N. M. Kronenberg, K. Ostermann, S. Ho fling, and M. C. Gather, Sci. Adv. 2, e1600666 (2016)
- ⁹⁹H. J. Oh, M. C. Gather, J. J. Song, and S. H. Yun, Opt. Express 22, 31411 (2014).
- ¹⁰⁰M. C. Gather and S. H. Yun, Nat. Photonics **5**, 406 (2011).